# Depletion of SMN Protein in Mesenchymal Progenitors Impairs the Development of Bone and Neuromuscular Junction in Spinal Muscular Atrophy

**Sang-Hyeon Hann[1]*, Seon-Yong Kim[2]*, Ye-Lynne Kim[1], Young-Woo Jo[1], Jong-Seol Kang[1], Hyerim Park[1], Se-Young Choi[2#] and Young-Yun Kong[1#]**

[1]School of Biological Sciences, Seoul National University, Seoul 08826, Republic of Korea

[2]Department of Physiology, Dental Research Institute, Seoul National University School of Dentistry, Seoul, 03080, Republic of Korea

[3]

*These authors contributed equally to this work

[#]Correspondence and requests for materials should be addressed to Y.Y.K. (ykong@snu.ac.kr) and S.Y.C. (sychoi@snu.ac.kr)

**Abstract**

Spinal Muscular Atrophy (SMA) is a neuromuscular disorder characterized by the deficiency of the survival motor neuron (SMN) protein, which leads to motor neuron dysfunction and muscle atrophy. In addition to the requirement for SMN in motor neurons, recent studies suggest that SMN deficiency in peripheral tissues plays a key role in the pathogenesis of SMA. Using limb mesenchymal progenitor cells (MPCs)-specific SMN-depleted mouse models, we reveal that SMN reduction in chondrocytes and fibro-adipogenic progenitors (FAPs) derived from limb MPCs causes defects in the development of bone and neuromuscular junction (NMJ), respectively. We show that impaired growth plate homeostasis, which causes skeletal growth defects in SMA, is cell-autonomous due to SMN ablation in chondrocytes. Furthermore, the reduction of SMN in FAPs resulted in abnormal NMJ maturation, altered release of neurotransmitters, and NMJ morphological defects. Transplantation of healthy FAPs rescued the morphological deterioration. Our findings highlight the significance of mesenchymal SMN in neuromusculoskeletal pathogenesis in SMA and provide insights into potential therapeutic strategies targeting mesenchymal cells for the treatment of SMA.

## Introduction

The survival motor neuron (SMN) protein is a crucial component of the spliceosome complex and is essential for the proper function of all cell types (Mercuri et al., 2022). Deficiency in SMN protein disrupts the formation of spliceosome complexes, ultimately causing splicing defects in multiple genes. Mutations in the SMN1 gene, which encodes the SMN protein, give rise to the neuromuscular disorder Spinal Muscular Atrophy (SMA). SMA is characterized by neuromuscular junctions (NMJ) disruption, muscular atrophy, and alpha motor neuron loss (Mercuri et al., 2022; Burghes et al., 2009). The severity of the disease in humans correlates with the copy number of SMN2, which is a paralog of SMN1 in humans. SMN2 primarily produces less functional exon 7-deleted SMN protein and rarely generates a limited quantity of functional full-length SMN protein via alternative splicing. SMA patients are classified into types 0 through 4 based on the severity and timing of disease onset, predominantly determined by the number of copies of the SMN2 gene they possess. More than 50% of SMA patients are categorized as type 1, characterized by muscle defects with proximal muscle atrophy during infancy, eventually resulting in death within a few years (Mercuri et al., 2022).

Previous studies suggest that the onset of SMA is mainly attributed to SMN loss in motor neurons (Monani et al., 2000; Burghes et al., 2009). Nevertheless, motor neuron-specific SMN deficiency in the SMA mouse model exhibits relatively mild phenotypes compared to whole-body SMA mouse models (Park et al., 2010; McGovern et al., 2015). Furthermore, restoring SMN to motor neurons in SMA mouse models result in only partial rescue in lifespan and neuromuscular defects (Passini et al., 2010; Martinez et al., 2012; McGovern et al., 2015; Besse et al., 2020). Systemic administration of antisense oligonucleotide (ASO),

58 which corrects SMN2 splicing to restore SMN expression, significantly prolongs survival
59 compared to CNS administration (Hua et al., 2011). In the mouse treated with a systemically
60 delivered ASO, blocking the effect of ASO in the CNS by a complementary decoy did not
61 have any detrimental effect on survival, motor function, or NMJ integrity (Hua et al., 2015).
62 These studies suggest that peripheral SMN plays a crucial part in SMA pathology. Overall,
63 investigating the impacts of SMN depletion in peripheral tissues is critical for alleviating
64 neuromuscular impairments and increasing life expectancy in SMA.

65 In SMA patients, bone growth retardation has been observed (Khatri et al., 2008; Vai et al.,
66 2015; Wasserman et al., 2017; Baranello et al., 2019; Hensel et al., 2020). Studies using
67 whole-body SMA mouse models have revealed that this is caused by diminished growth plate
68 chondrocyte proliferation and extracellular matrix (ECM) remodeling defects, independent of
69 muscle atrophy (Hensel et al., 2020). However, it is still unclear whether these defects result
70 from an internal factor such as SMN ablation in chondrocytes, or an external factor such as
71 IGF1 decline in SMA patients and mice (Hua et al., 2011; Yesbek-Kaymaz et al., 2016).

72 Mesenchymal progenitor cells (MPCs) derived from the lateral plate mesoderm (LPM)
73 differentiate into various types of limb mesenchymal cells, including bone, cartilage, and
74 intramuscular mesenchymal cells like fibro-adipogenic progenitors (FAPs) (Nassari et al.,
75 2017). Recent studies have revealed the role of FAPs in skeletal muscle homeostasis, as
76 reducing the number of FAPs resulted in diminished muscle regeneration capacity, long-term
77 muscle atrophy, and NMJ denervation (Wosczyna et al., 2019; Uezumi et al., 2021). Our
78 latest research demonstrated that FAPs-specific deficiency of Bap1, one of the
79 deubiquitinases, leads to NMJ defects (Kim et al., 2022). These recent findings raise the
80 possibility that FAPs may have a specific role in the pathogenesis of neuromuscular diseases

such as SMA. However, it has not been studied if depletion of SMN in FAPs can lead to SMA-like neuromuscular pathology.

In this study, we crossed a limb MPCs-specific Cre mouse with a floxed Smn exon7 mouse carrying multiple copies of the human SMN2 gene, allowing us to examine the impact of mesenchymal SMN reduction on SMA pathogenesis. Our findings indicate that the SMN reduction in FAPs, similar to the extent of severe SMA, causes altered NMJ development like SMA. Additionally, in chondrocytes, it leads to skeletal growth abnormalities due to growth plate cell-autonomous defects.

## Results

### Bone growth restriction due to growth plate cell-autonomous defects caused by MPCs-specific SMN depletion

To investigate the effects of SMN reduction within MPCs in SMA pathogenesis, we crossed *Smn*$^{f7/f7}$ mice, which possess loxP sites flanking exon 7 of the Smn gene (Frugier et al., 2000), with *Prrx1*$^{Cre}$ mice. This produced Smn$^{\Delta MPC}$ mice (*Prrx1*$^{Cre}$*; Smn*$^{f7/f7}$) that lacked the Smn gene specifically in Prrx1$^{Cre}$-expressed limb MPCs that give rise to bone, cartilage, and FAPs (Logan et al., 2002; Leinroth et al., 2022). To ascertain whether mutant mice carrying the SMN2 gene, like SMA patients, present pathological phenotypes, we additionally generated SMN2 2-copy Smn$^{\Delta MPC}$ (*Prrx1*$^{Cre}$*; Smn*$^{f7/f7}$*; SMN2*$^{+/+}$) and SMN2 1-copy Smn$^{\Delta MPC}$ (*Prrx1*$^{Cre}$*; Smn*$^{f7/f7}$*; SMN2*$^{+/0}$) mice. Control littermates that lacked Prrx1$^{Cre}$ were used as controls for comparison.

SMN2 0-copy Smn$^{\Delta MPC}$ mice died within 24 hours after birth. Regions where limbs should

103 have formed at E18.5 only had rudimentary limb structures (Figure 1—figure supplement
104 1A). Furthermore, since the upper head bone did not envelop the brain, it was directly
105 attached to the skin and protruded. These observations can be attributed to Prrx1$^{Cre}$-mediated
106 SMN deletion in the LPM-derived limb MPCs and the craniofacial mesenchyme, which is
107 accountable for the formation of calvarial bone (Wilk et al., 2017). To investigate whether the
108 lack of SMN proteins in MPCs is responsible for bone development abnormalities, we
109 performed alcian blue and alizarin red staining on E18.5 SMN2 0-copy Smn$^{\Delta MPC}$ mutants to
110 analyze the structure of bones and cartilage. The appendages displayed restricted bone and
111 cartilage formations, with scarcely discernible femur and tibia (Figure 1—figure supplement
112 1B-C). In the cranial region, there was an absence of both cartilage and bone at the location
113 of the calvarial bone, with the parietal bone entirely missing and partially absent frontal bone
114 (Figure 1—figure supplement 1D). Additionally, the sternum, which is one of the bones
115 originating from the LPM (Sheng et al., 2015), was shorter than the control (Figure 1—figure
116 supplement 1E).

117 The SMN2 2-copy Smn$^{\Delta MPC}$ mice, carrying two homologous SMN2 genes, did not show any
118 discernible differences from the Prrx1$^{Cre}$-negative control littermates into adulthood.
119 However, the SMN2 1-copy Smn$^{\Delta MPC}$ mice exhibited reduced body size and shorter limb
120 length compared to the SMN2 1-copy control (Smn$^{f7/f7}$; SMN2$^{+/0}$). To assess postnatal bone
121 growth defects observed in SMA patients and mouse models, we conducted micro-CT
122 analysis on femurs obtained from postnatal day 14 (P14) SMN2 1-copy Smn$^{\Delta MPC}$ and SMN2
123 2-copy Smn$^{\Delta MPC}$ mice (Figure 1A). The data showed that SMN2 1-copy mutants exhibited
124 reduced femur diaphysis length, diameter, and trabecular bone volume compared to the
125 control group, indicating bone formation defects (Figure 1B-D). We then examined femoral

126 bone thickness and diaphyseal bone mineral density (BMD) to determine whether
127 mineralization was normal after bone formation. The thickness of the bone in the mutants did
128 not differ significantly from the control, suggesting that bone mineralization was intact
129 (Figure 1—figure supplement 1E-F). Unexpectedly, BMD slightly increased in SMN2 1-copy
130 mutants compared to the control group (Figure 1—figure supplement 1G). The higher BMD
131 may be attributed to greater mechanical stress caused by the shorter femur supporting the
132 weight of the body, consistent with prior research indicating that elevated mechanical force
133 leads to higher BMD in the femur (Hoxha et al., 2014; Ike et al., 2015). Nevertheless, the
134 decrease in bone growth without apparent deterioration in bone mineralization of the femur
135 of SMN2 1-copy $Smn^{\Delta MPC}$ mutants is consistent with findings from the whole-body SMA
136 mouse model (Hensel et al., 2020). Collectively, these results suggest that mice carrying low
137 copies of SMN2, with the SMN gene specifically deleted in MPCs, exhibit bone growth
138 defects.

139 To determine whether bone growth defects in SMN2 1-copy $Smn^{\Delta MPC}$ mutants arise from
140 disrupted chondrocyte homeostasis at growth plates, we stained the femur growth plate of
141 P14 mice with hematoxylin and eosin (Figure 1—figure supplement 2A). In line with earlier
142 findings in whole-body SMA mice (Hensel et al., 2020), SMN2 1-copy $Smn^{\Delta MPC}$ mice
143 exhibited shorter proliferative and hypertrophic zones compared to control mice (Figure 1—
144 figure supplement 2B-D). Additionally, there was a significant reduction in the number of
145 chondrocytes in the hypertrophic zone (Figure 1—figure supplement 1J). Our data indicate
146 that adequate expression of SMN is essential for the homeostasis of chondrocytes at growth
147 plates.

148

149 **Mesenchymal cell-specific SMN reduction similar to severe SMA mouse model in SMN2**
150 **1-copy Smn$^{\Delta MPC}$ mutants**

151 The proliferation and differentiation of growth plate chondrocytes are regulated by extrinsic
152 factors such as GH-IGF-I, glucocorticoids, and estrogen (Shim et al., 2015; Karimian et al.,
153 2012; Shantanam et al., 2018). Previous research indicates that reduced expression of Igf-
154 I/Igfbp3/Igfals in the liver leads to impaired chondrocyte proliferation and shorter femur
155 length, emphasizing the importance of these factors in postnatal bone development (Yakar et
156 al., 2002; Yakar et al., 2009). As the IGF pathway proteins are downregulated in whole-body
157 SMA mice, the bone growth defects observed in the mice have sparked debate as it remains
158 unclear whether they are due to intrinsic factors, such as chondrocyte SMN reduction, or the
159 low IGF axis level (Hua et al., 2011; Tsai et al., 2014; Deguise et al., 2021; Hensel et al.,
160 2015).

161 To clarify this issue, we used Smn$^{\Delta MPC}$ mutant mice, which enabled us to investigate the
162 effect of SMN depletion in chondrocytes on bone growth, while circumventing the impact of
163 external factors. To confirm the specific deletion of Smn in limb mesenchymal cells,
164 including chondrocytes and FAPs, we performed qRT-PCR for full-length Smn mRNA
165 expression in each tissue. Our findings indicate that full-length Smn mRNA expression in the
166 brain, liver, skeletal muscle, and spinal cord of SMN2 1-copy Smn$^{\Delta MPC}$ mice at postnatal day
167 21 (P21) was similar to that of control mice, while it was significantly reduced in isolated
168 FAPs and chondrocytes (Figure 1I). Additionally, we confirmed the presence of the SmnΔ7
169 variant, which is the exon 7-deleted form of Smn created by cre-lox mediated recombination,
170 in both FAPs and chondrocytes by conducting genomic PCR on the SMN2 1-copy Smn$^{\Delta MPC}$
171 mutant (Figure 1H). Since SMN was not down-regulated in the tissues other than limb

172 mesenchymal cells, non-mesenchymal cells were ruled out from being responsible for the
173 phenotype observed in $Smn^{\Delta MPC}$ mutants. Indeed, the liver's mRNA expression of IGF
174 pathway genes, reported to be decreased in SMA mouse models and patients (Hua et al., 2011;
175 Deguise., 2021; Sahashi et al., 2013), showed no difference when comparing controls to
176 SMN2 1-copy $Smn^{\Delta MPC}$ mutants (Figure 1—figure supplement 2E). Based on these findings,
177 we concluded that the bone growth defects observed in the whole-body SMA mouse model
178 are mainly due to a depletion of SMN in chondrocytes.

179 Among our $Smn^{\Delta MPC}$ models, mice with two copies of SMN2 exhibit similar bone
180 development parameters as control mice without SMN deletion. However, mice with one
181 copy of SMN2 display bone pathological defects akin to SMA mouse models. This may be
182 because the quantity of human full-length SMN protein produced by SMN2 2-copy, was
183 sufficient to sustain SMN complex function in the SMN2 2-copy $Smn^{\Delta MPC}$ mutants, despite
184 the absence of functional mouse SMN protein in limb mesenchymal cells. On the contrary,
185 due to the lower expression of full-length SMN compared to SMN2 2-copy mutants, the
186 SMN complex may not function properly in SMN2 1-copy mutant cells. We confirmed this
187 by comparing the amount of full-length SMN protein in isolated FAPs from the hindlimbs of
188 control, $Smn^{\Delta MPC}$ mutants, and a severe SMA mouse model (*$Smn^{-/-}$; $SMN2^{+/+}$; $SMN\Delta7^{+/+}$*; -
189 SMAΔ7 mutants -) (Figure 1I). The data show that SMN2 1-copy $Smn^{\Delta MPC}$ mutants exhibited
190 ~80% reduction in SMN levels compared to the control group. The level of SMN protein in
191 SMN2 1-copy $Smn^{\Delta MPC}$ mutants was similar to that in SMAΔ7 mutants. Conversely, SMN2
192 2-copy mutants display a decrease of approximately 40% in SMN protein levels compared to
193 the control (Figure 1J). The moderately reduced expression of SMN is adequate to support
194 regular bone development in SMN2 2-copy mutants. Taken together, our findings indicate

195 that the reduction of mesenchymal SMN to levels comparable to that of the severe SMA
196 mouse model causes SMA-like bone pathology in the SMN2 1-copy mutant.

197

198 **Abnormal NMJ maturation in SMN2 1-copy Smn$^{\Delta MPC}$ mutants**

199 To investigate whether disabling SMN in FAPs results in SMA-like neuromuscular
200 impairments, we assessed if NMJ phenotypes observed in SMA mouse models also occur in
201 SMN2 1-copy Smn$^{\Delta MPC}$ mutants. Both severe and mild SMA mouse models exhibit impaired
202 NMJ maturation markers, including plaque-like morphology of acetylcholine receptor (AChR)
203 clusters, neurofilament (NF) varicosities, and poor terminal arborization (Kong et al., 2009;
204 Martinez, 2012; Monani et al., 2003; Kariya et al., 2008). To evaluate the impact of SMN
205 deficiency in FAPs on NMJ maturation, we evaluated the NMJ maturation markers in the TA
206 muscles of control and SMN2 1-copy Smn$^{\Delta MPC}$ mutant mice at P21, a time when NMJ
207 maturation is in progress (Figure 2A). Our examination revealed the presence of NF
208 varicosities in SMN2 1-copy mutants as compared with control mice (Figure 2A and 2D).
209 Additionally, the number of nerve branches was decreased and half of the total NMJs were
210 poorly arborized in SMN2 1-copy mutants (Figure 2B-C). These presynaptic alterations are
211 specific phenotypes in neurogenic atrophy like SMA. Unlike neurogenic atrophy, physiologic
212 atrophy shows no differences in presynaptic morphology, such as nerve branching
213 (Deschenes et al., 2006). This suggests that the NMJ phenotypes observed in SMN2 1-copy
214 Smn$^{\Delta MPC}$ mutant mice are not caused by decreased muscle size and activity resulting from
215 bone growth abnormalities. The morphology of AChR clusters shows that the mutants have
216 more immature plaque-like NMJs than the controls' pretzel-like structure (Figure 2E).
217 Therefore, these findings indicate that SMN2 1-copy Smn$^{\Delta MPC}$ mutants exhibit NMJ

218 maturation abnormalities common in SMA mouse models.

219

220 **Undisturbed NMJ formation in neonatal SMN2 1-copy Smn$^{\Delta MPC}$ mutants**

221 To determine whether any NMJ defects were present prior to juvenile NMJ maturation in
222 SMN2 1-copy Smn$^{\Delta MPC}$, we examined NMJ formation in SMN2 1-copy Smn$^{\Delta MPC}$ mice at the
223 neonatal stage on postnatal day 3. We evaluated the AChR and nerve terminal areas to assess
224 postsynaptic and presynaptic development, respectively (Figure 2F). Measurements of AChR
225 cluster size indicated no differences between control and SMN2 1-copy Smn$^{\Delta MPC}$ mice
226 (Figure 2G). However, the area of AChR covered by nerve terminals was slightly larger in
227 SMN2 1-copy Smn$^{\Delta MPC}$ (Figure 2H). We have no reasonable explanation for why the
228 coverage is higher in the mutant. However, there does not appear to be abnormal
229 development of the NMJ in the mutant, at least until the neonatal period. Therefore, we
230 reasoned that SMN2 1-copy Smn$^{\Delta MPC}$ mutants began to exhibit deterioration in the NMJ
231 maturation during the juvenile stage, following the intact neonatal development of NMJ.

232

233 **Aberrant NMJ morphology in the adult SMN2 1-copy Smn$^{\Delta MPC}$ mice**

234 To evaluate the organization of NMJ after the conclusion of postnatal NMJ development,
235 considering mesenchymal SMN expression, we examined NMJ morphology in the TA muscle
236 of control, SMN2 1-copy, and 2-copy Smn$^{\Delta MPC}$ mice at postnatal day 56 (P56). Our analysis
237 revealed that presynapses were fragmented in SMN2 1-copy mutants, resulting in a bouton-
238 like morphology, in contrast to the control and SMN2 2-copy Smn$^{\Delta MPC}$ mice (Figure 3A). In
239 SMN2 1-copy Smn$^{\Delta MPC}$ mice, a two-fold presynaptic fragmentation compared to the control

240 was quantified, demonstrating nerve terminal shrinkage (Figure 3B). Additionally, NF ends
241 displayed more severe varicosities than at P21 and were only connected to the proximal nerve
242 by very thin NF, unlike control and SMN2 2-copy mice (Figure 3C). Remarkably, numerous
243 presynaptic islands formed in SMN2 1-copy $Smn^{\Delta MPC}$ mice through the merging of
244 fragmented presynapses and NF varicosity. In SMN2 1-copy mutants, AChR clusters
245 displayed fragmented grape-shaped morphology that overlapped with nerve terminals,
246 whereas control and SMN2 2-copy mice displayed pretzel-like structures (Figure 3D). These
247 results suggest that defects in adult NMJ morphology occur when mesenchymal SMN protein
248 is reduced to the extent of the SMN2 1-copy $Smn^{\Delta MPC}$ mutants.

249

250 **Presynaptic neurotransmission alteration in SMN2 1-copy $Smn^{\Delta MPC}$ mutants**

251 To investigate whether the morphologically aberrant NMJs of SMN2 1-copy $Smn^{\Delta MPC}$ mice
252 have functional impairments, we isolated hindlimb extensor digitorum longus (EDL) muscles
253 from P56 mice and conducted electrophysiological recording. We incubated the muscles with
254 μ-conotoxin, which selectively inhibits muscle voltage-gated Na+ channels, prevented the
255 induction of muscle action potential (Ling et al., 2010; Zanetti 2018), and recorded the
256 Miniature endplate potential (mEPP) and evoked endplate potential (eEPP). (Ling et al., 2010;
257 Zanetti 2018). mEPP, a response that occurs when spontaneously released acetylcholine binds
258 to nicotinic AChR without nerve stimulation, was measured ex vivo near the NMJs of the
259 EDL muscles in the control and SMN2 1-copy $Smn^{\Delta MPC}$ mice (Figure 4A). The mEPP
260 amplitude was increased in SMN2 1-copy $Smn^{\Delta MPC}$ mice (Figure 4B), whereas mEPP
261 frequency was comparable between the controls and mutants (Figure 4C). The results
262 indicate that the NMJ synapses of SMN2 1-copy $Smn^{\Delta MPC}$ mice are functional and more

263 sensitive to acetylcholine compared to the controls. Next, we measured the eEPP by
264 stimulating an action potential at the peroneal nerve (Figure 4D). Despite the increased mEPP
265 amplitude, the amplitude of eEPPs was significantly decreased in SMN2 1-copy $Smn^{\Delta MPC}$
266 mice (Figure 4E). These results suggest that the nerve terminals in SMN2 1-copy $Smn^{\Delta MPC}$
267 mice exhibit decreased quantal content. This could be due to a decrease in vesicle release
268 probability or a reduced readily releasable pool (RRP). Notably, there was no difference in
269 the paired-pulse response, indicating normal neurotransmitter release probability (Figure 4F).
270 Taken together, these findings suggest that the presynaptic neurotransmission ability of the
271 NMJ is reduced in SMN2 1-copy $Smn^{\Delta MPC}$ mutants.

272

273 **Disturbed nerve terminal structure in SMN2 1-copy $Smn^{\Delta MPC}$ mice**

274 To examine the NMJ ultrastructure of SMN2 1-copy $Smn^{\Delta MPC}$ mutants, we utilized
275 transmission electron microscopy (TEM) (Figure 5A). The density of junctional folds in
276 SMN2 1-copy $Smn^{\Delta MPC}$ mutant specimens was comparable to that of the control (Figure 5B).
277 However, the density of synaptic vesicles was substantially elevated in the SMN2 1-copy
278 mutants (Figure 5C). Since previous electrophysiological results suggested a decrease in
279 presynaptic neurotransmission capacity in SMN2 1-copy mutants, this could be due to
280 synaptic vesicles failing to fuse with the membrane, leading to the accumulation of vesicles
281 in the terminal. Additionally, the detachment of the nerve terminal is more frequent at the
282 NMJ of mutants (Figure 5D). The detachment of nerve terminals observed in SMN2 1-copy
283 $Smn^{\Delta MPC}$ mutants could have resulted in diminished presynaptic neurotransmission capacity.
284 Collectively, these findings indicate that SMN2 1-copy $Smn^{\Delta MPC}$ mutants have nerve

285 terminal-specific pathological defects at the NMJ ultrastructural level.

286

287 **FAPs transplantation rescues NMJ morphology in limb mesenchymal SMN mutants**

288 SMN-deleted limb mesenchymal tissues in SMN2 1-copy $Smn^{\Delta MPC}$ mutants comprise not
289 only FAPs, but also bone, cartilage, pericytes, and tendon, among others (Leinroth et al.,
290 2022; Nassari et al., 2017). To evaluate the critical role of FAPs in the postnatal development
291 of the NMJ, we isolated fluorescent protein-labeled wild-type FAPs from $Prrx1^{Cre}$;
292 $Rosa26^{YFP/+}$ or $Prrx1^{Cre}$; $Rosa26^{tdTomato/+}$ mice and transplanted them into the TA muscles of
293 SMN2 1-copy $Smn^{\Delta MPC}$ mice at postnatal day 10. The TA muscle on the contralateral side
294 was treated with a vehicle as a control. In SMN2 1-copy $Smn^{\Delta MPC}$ mice at P56, the muscle
295 that received FAPs showed decreased presynaptic fragmentation, NF varicosities, and
296 postsynaptic fragmentation compared to the contralateral muscle (Figure 6A-D). These data
297 demonstrate that the transplantation of wild-type FAPs rescues the abnormal NMJ
298 development in SMN2 1-copy $Smn^{\Delta MPC}$ mice. Overall, our findings indicate that SMN
299 depletion in FAPs leads to the neuronal SMN-independent NMJ pathology in severe SMA,
300 which is rescued by the transplantation of healthy FAPs.

301

302 **Discussion**

303 In this paper, we elucidate the contribution of SMN depletion in mesenchymal progenitors for
304 the pathogenesis of SMA. To test this hypothesis, we generated conditional knockout mouse
305 strains to delete the Smn allele specifically in limb mesenchymal cells and carry human
306 SMN2 copies. Our research using these mouse models resulted in three major discoveries.

307 First, SMN deficiency in FAPs contributes to NMJ pathological defects in SMA. We
308 observed delayed NMJ maturation and varicosities in juvenile SMN2 1-copy $Smn^{\Delta MPC}$
309 mutant. The pathogenic NMJ phenotypes were also observed in the SMAΔ7 mutant, which is
310 one of the severe SMA mouse models (Kong et al., 2009; Martinez, 2012; Kariya et al., 2008).
311 As the SMAΔ7 mutant typically lives for approximately 12 days, the fragmentation of the
312 NMJ in adult SMN2 1-copy mutant was not evaluated in the severe SMA mutant.
313 Nevertheless, models that induce a conditional adult SMN deficiency through either $Cre^{ER}$
314 allele or oligonucleotide administration resulting in SMN reduction, demonstrated the
315 depletion of SMN throughout the body caused fragmentation of NMJ (Sahashi et al., 2013;
316 Kariya et al., 2014). Thus, we demonstrate that the SMN2 1-copy $Smn^{\Delta MPC}$ mutant model
317 mimics whole-body SMA mouse models in NMJ morphology. In the electrophysiological test,
318 the SMAΔ7 mutant exhibited reduced quantal content, readily releasable pool (RRP), and
319 vesicle release probability (Torres-Benito et al., 2011). In our study, we did not assess RRP in
320 SMN2 1-copy $Smn^{\Delta MPC}$ mutant, but instead reduced quantal content and normal vesicle
321 release probability, indicating a reduced RRP size. The decrease in RRP size in the SMAΔ7
322 mutant was attributed to abnormal axonal transport, which led to a decline in synaptic vesicle
323 density in the nerve terminal (Dale et al., 2011; Kong et al., 2009). However, we found that
324 synaptic vesicle density was increased in the SMN2 1-copy $Smn^{\Delta MPC}$ mutant. It is possible
325 that the alteration of active zones, which were observed in the SMA motor terminals,
326 contributed to the reduction in synaptic vesicle fusion and the higher synaptic vesicle density.
327 Indeed, nerve terminal detachment in SMN2 1-copy mutant mice was also found in active
328 zone complex protein integrin-α3 knockout mice (Ross et al., 2017). Based on the rescue data
329 of transplanted healthy FAPs, we can report that FAPs-specific SMN depletion is involved in
330 NMJ pathology of SMA.

331 Second, we demonstrated that skeletal growth defects, a phenotype observed in SMA (Khatri
332 et al., 2008; Vai et al., 2015; Wasserman et al., 2017; Baranello et al., 2019; Hensel et al.,
333 2020), are a cell-autonomous pathological effect of the depletion of SMN in chondrocytes.
334 We observed reduced bone size and volume in juvenile SMN2 1-copy $Smn^{\Delta MPC}$ mutant.
335 Depletion of SMN from chondrocytes is sufficient to cause growth problems without altering
336 the hepatic IGF axis, which affects growth plate homeostasis. Recent studies have reported
337 that IGF1 overexpression improves biochemical and behavioral manifestations in SMA mice,
338 suggesting potential therapies for SMA (Bosch-Marce et al., 2011; Tsai et al., 2014). Our
339 study demonstrated that these IGF1 therapies for SMA without mesenchymal SMN
340 supplementation have a limited ability to rescue bone abnormalities. In addition, the skeletal
341 growth defect may affect physiologic muscle atrophy through imbalanced muscle contraction
342 and reduced tension. This physiologic atrophy may be part of SMA-associated muscle
343 weakness independent of neurogenic atrophy.

344 Third, it was demonstrated that adequate levels of SMN protein are essential for MPCs to
345 contribute to limb neuromusculoskeletal development. The mutants with only 1 copy of
346 SMN2 exhibit problematic symptoms observed in both SMA patients and mouse models,
347 while SMN2 2-copy mutants display a typical phenotype in bone and NMJ. The lack of SMN
348 protein in MPCs by insufficient SMN2 copies, similar to the deficiency seen in severe SMA,
349 is responsible for the onset of SMA pathology. Thus, we propose that restoration of deficient
350 SMN in MPCs is crucial for rehabilitating their function. Based on these discoveries, SMN
351 replenishment treatments for MPCs, specifically FAPs, and chondrocytes, are necessary to
352 provide a complete solution for neuromusculoskeletal defects in severe SMA patients.

353 The initial focus for the treatment of SMA was on motor neurons located in the spinal cord,

354 and pharmaceuticals were created to address the deficiency of SMN in these neurons
355 (Mercuri et al., 2020). For example, intrathecal injections of Spinraza can efficiently boost
356 SMN in the CNS, including the spinal cord (Passini et al., 2011; Claborn et al., 2018).
357 However, Spinraza does not address the lack of SMN in peripheral tissues, including
358 mesenchymal cells, highlighted in recent studies. The drug Zolgensma, which employs AAV9
359 to express SMN through systemic delivery, appears to resolve this issue (Foust et al., 2009;
360 Foust et al., 2022; Valori et al., 2010; Mattar et al., 2013). Nevertheless, a prior study
361 indicates that chondrocytes within the growth plate and articular cartilage do not get infected
362 with AAV9 (Yang et al., 2019). Furthermore, it is well-established that DNA vectors
363 delivered via AAV9 undergo dilution during cell proliferation (Penaud-Budloo et al., 2008;
364 Colella et al., 2018; Van-Alstyne et al., 2021; Heller et al., 2021). Given the infection issue
365 and the dilution issue by the active cell population changes of chondrocytes and FAPs during
366 postnatal development (Petrany., 2020; Bachman et al., 2022), SMN supplementation through
367 Zolgensma alone would not be sufficient for severe SMA patients. Thus, there is an urgent
368 need to research and develop therapeutic strategies that target mesenchymal progenitors.

369 While this study is the first to demonstrate the impact of SMN depletion in FAPs on the NMJ
370 development, it does not elucidate the specific mechanism by which FAPs influence the NMJ.
371 Our study observed NMJ recovery in the muscles transplanted with healthy FAPs, but not in
372 the contralateral muscles, indicating that FAPs are likely involved in NMJ development
373 through juxtacrine or paracrine signaling. Since FAPs interact with surrounding tissues
374 through a variety of signaling factors, such as extracellular matrix (Contreras et al., 2021;
375 Scott et al 2019), Wnt-related protein (Lukjanenko et al., 2019), and Bmp signaling protein
376 (Uezumi et al., 2021; Camps et al., 2020), mis-splicing of the signaling factors due to SMN

377 reduction could disturb the homeostasis of neighboring tissues (Zhang et al., 2008).
378 Furthermore, a population of FAPs associated with NMJ was discovered through single-cell
379 RNA sequencing in a recent study (Leinroth et al., 2022). This population is located adjacent
380 to the NMJ and responds to denervation, indicating an increased possibility of interaction
381 with the NMJ organization. Therefore, it is necessary to conduct additional investigations into
382 the expression of various signaling factors by diverse FAP populations in future studies.

383

## Methods

### Animals

*Prrx1*$^{Cre}$ (stock 005584), *Smn*$^{f7/+}$ (stock 006138), *Rosa26*$^{YFP/+}$ (stock 006148), *Rosa26*$^{tdTomato/+}$ (stock 007914), *SMN2*$^{+/+}$, *Smn*$^{+/-}$ (stock 005024) and *Smn*$^{+/-}$*; SMN2*$^{+/+}$*; SMNΔ7*$^{+/+}$ (stock 005025) mice were acquired from The Jackson Laboratory (Bar Harbor, ME, USA). SMN2 0-copy Smn$^{\Delta MPC}$ mice (*Prrx1*$^{Cre}$*; Smn*$^{f7/f7}$), SMN2 1-copy Smn$^{\Delta MPC}$ mice (*Prrx1*$^{Cre}$*; Smn*$^{f7/f7}$*; SMN2*$^{+/0}$), and SMN2 2-copy Smn$^{\Delta MPC}$ mice (*Prrx1*$^{Cre}$*; Smn*$^{f7/f7}$*; SMN2*$^{+/+}$) were generated by crossing *Prrx1*$^{Cre}$ mice with *Smn*$^{f7/+}$ and *Smn*$^{+/-}$*; SMN2*$^{+/+}$mice. To utilize fibro-adipogenic progenitors (FAPs) transplantation, we generated *Prrx1*$^{Cre}$*; Rosa26*$^{YFP/+}$ mice and *Prrx1*$^{Cre}$*; Rosa26*$^{tdTomato/+}$ mice by breeding *Prrx1*$^{Cre}$ with *Rosa26*$^{YFP/+}$ and *Rosa26*$^{tdTomato/+}$ mice, respectively. To avoid deletion of the floxed allele by *Prrx1*$^{Cre}$ expression in female germline, we bred females without *Prrx1*$^{Cre}$ line to *Prrx1*$^{Cre}$ transgenic males. SMAΔ7 mutants (*Smn*$^{-/-}$*; SMN2*$^{+/+}$*; SMNΔ7*$^{+/+}$) were produced by mating *Smn*$^{+/-}$*; SMN2*$^{+/+}$*; SMNΔ7*$^{+/+}$ mice. Both male and female mice were used in the experiments, and no sex-specific differences were observed. Control littermates lacking *Prrx1*$^{Cre}$ were utilized for analysis. All mouse lines were housed under controlled conditions with specific pathogen-free and handled according to the guidelines of the Seoul National University Institutional Animal Care and Use Committee (IACUC).

### Micro CT

The femurs from three groups - control, SMN2 2-copy Smn$^{\Delta MPC}$, and SMN2 1-copy Smn$^{\Delta MPC}$ mice at postnatal day 14 (P14) - were isolated and cleaned of muscles and skin. Subsequently,

406 the femurs were preserved in 4% paraformaldehyde (PFA) in PBS overnight at 4°C before
407 micro-computed tomography (micro CT). The femurs were then imaged through a Quantum
408 GX II micro-CT imaging system (PerkinElmer, Hopkinton, MA, USA). The X-ray source for
409 scanning was set at 90 kV and 88 mA with a field of view of 10 mm (voxel size, 20 μm;
410 scanning time, 14 min). The 3D imaging was viewed using the 3D Viewer software of the
411 Quantum GX II. The size and volume of the femur bone were measured via AccuCT analysis
412 software within the ossified diaphysis and metaphysis of the femur, excluding the epiphysis.
413 Bone mineral density (BMD) calibration was performed using a 4.5 mm BMD phantom and
414 BMD measurements were taken at the center of the diaphysis.

415

416 **Histology**

417 Alcian blue & alizarin red staining was performed on control and SMN2 0-copy $Smn^{\Delta MPC}$
418 mice at E18.5 using a previously reported protocol (Ovchinnikov, 2009). For hematoxylin &
419 eosin staining of the growth plate in the control and SMN2 1-copy $Smn^{\Delta MPC}$ mice at P14, the
420 femurs were fixed in 4% paraformaldehyde for 24 hours, rinsed in running tap water for 24
421 hours, and incubated with 10% EDTA (pH 7.4) at 4°C with shaking for 2-3 days.
422 Subsequently, the samples were rinsed in running tap water for 24 hours and then dehydrated
423 through ethanol/xylene and embedded in paraffin. The embedded samples were then
424 sectioned to a thickness of 5 μm, rehydrated, and stained with Gill No. 3 formula
425 hematoxylin and eosin Y (H&E, Sigma Aldrich, St. Louis, MO, USA). Stained slides were
426 analyzed using 10× and 20x objectives in the EVOS M7000 imaging system (Thermo Fisher
427 Scientific, Waltham, MA, USA). The growth plate's proliferative and hypertrophic zones
428 were defined by their respective cell sizes.

429

430 **Hindlimb fibro-adipogenic progenitors isolation**

431 Isolation of limb muscle FAPs was performed according to a previously reported protocol
432 (Kim et al., 2021) with modifications. Limb muscles were dissected and mechanically
433 dissociated in Dulbecco's modified Eagle's medium (DMEM, Hyclone) containing 10%
434 horse serum (Hyclone, Logan, UT, USA), collagenase II (800 units/mL; Worthington,
435 Lakewood, NJ, USA), and dispase (1.1 units/mL; ThermoFisher Scientific, Waltham, MA,
436 USA) at 37°C for 40 min. Digested suspensions were subsequently triturated by sterilized
437 syringes with 20G 1/2 needle (BD Biosciences, Franklin Lakes, NJ, USA) and washed with
438 DMEM to harvest mononuclear cells. Mononuclear cells were stained with corresponding
439 antibodies. All antibodies used in FACS analysis were listed in Supplemental Table 1. To
440 exclude dead cells, 7AAD (Sigma Aldrich; St. Louis, MO, USA) was used. Stained cells
441 were analyzed and $7AAD^{-}Lin^{-}Vcam^{-}Sca1^{+}$ (FAPs) were isolated using FACS Aria III cell
442 sorter (BD Biosciences) with 4-way-purity precision. For western blot, freshly isolated FAPs
443 were cultured at 37 °C in alpha-MEM (Hyclone) supplemented with Antibiotic-Antimycotic
444 (anti-anti, Gibco) and 20% FBS (Hyclone). For transplantation, $YFP^{+}$ FAPs and $tdTomato^{+}$
445 FAPs were isolated from postnatal day 10~21 *Prrx1*$^{Cre}$; *Rosa26*$^{YFP/+}$ mice and *Prrx1*$^{Cre}$;
446 *Rosa26*$^{tdTomato/+}$ mice, respectively. Isotype control density plots were used as a reference for
447 positive gating.

448

449 **Chondrocytes isolation**

450 Isolation of chondrocytes followed a modified protocol previously published (Jonason et al.,

451 2015). Using blunt forceps, cartilage caps were removed from P21 mouse femoral heads and
452 dissected into ~1mm fragments in a petri dish with 10X anti-anti in PBS. The cartilage
453 fragments were washed twice with PBS and then incubated in 5 mL collagenase II solution
454 (800 units/mL collagenase II in DMEM with 1X anti-anti, sterilized by 0.2 μm filtration) in a
455 60-mm culture dish at 37 °C in a 5% CO2 incubator overnight. Chondrocytes were released
456 by pipetting the remaining cartilage fragments ten times and then filtering them through a 70
457 μm cell strainer to a 50 ml conical tube. The cells were then washed twice with PBS and
458 pelleted by centrifugation at 500g for 5 min. Subsequently, the cells were cultured overnight
459 at 37 °C in a 5% CO2 incubator, in complete culture medium (DMEM with 10% FBS and 1X
460 anti-anti) overnight at 37 °C in a 5% CO2 incubator.

461

462 **PCR reaction**

463 To detect the presence of Smn exon 7 floxed and deleted allele, 20 mg of each tissue were
464 dissolved in direct PCR buffer (VIAGEN) with proteinase K overnight at 65°C. After
465 inactivation at 95°C for 30 minutes, PCR was performed using previously reported primer
466 sets to verify the existence of Cre, $Smn^{f7}$, and $Smn^{\Delta 7}$ alleles (Frugier et al., 2000). Primers are
467 listed in Supplemental Table 1.

468

469 **RNA extraction and measurement of mRNA expression**

470 Total RNA was extracted from the brain, liver, spinal cord L4, tibialis anterior muscle, freshly
471 isolated FAPs, and chondrocytes using a TRIzol Reagent (Life Technologies, Carlsbad, CA,
472 USA) and analyzed by qRT-PCR. First-strand complementary DNA was synthesized from 1

473 μg of RNA using ReverTra Ace (Toyobo, Osaka, Japan) containing random oligomer
474 according to the manufacturer's instructions. qRT-PCR (Qiagen) was performed with SYBR
475 Green technology (SYBR Premix Ex Taq, Qiagen) using specific primers against indicated
476 genes. Relative mRNA levels were determined using the $2^{-\Delta\Delta Ct}$ method and normalized to
477 *Gapdh* (Figure 1H, Figure 1—figure supplement 1K). Primers are listed in Supplemental
478 Table 1.

479

480 **Western blot**

481 Cultured FAPs at passage 3 were homogenized in RIPA buffer (50 mM Tris-HCl, pH 7.5, 0.5%
482 SDS, 20 μg/ mL aprotinin, 20 μg/ mL leupeptin, 10 μg/ mL phenylmethylsulfonyl fluoride, 1
483 mM sodium orthovanadate, 10 mM sodium pyrophosphate, 10 mM sodium fluoride, and 1
484 mM dithiothreitol). Cell lysates were centrifuged at 13,000 rpm for 15 min. Supernatants
485 were collected and subjected to immunoblot. BCA protein assay (Thermo Fisher Scientific)
486 was used for estimating total protein concentrations. Normalized total proteins were analyzed
487 by electrophoresis in 10% polyacrylamide gels and transferred to PVDF membranes
488 (Millipore, Billerica, MA, USA). Membranes were blocked in 5% skim milk (BD
489 Biosciences) in TBS with 0.1% Tween-20 and incubated with primary antibodies overnight at
490 4°C. After incubation with the corresponding HRP-conjugated secondary antibodies, the
491 membranes were developed using a Fusion solo chemiluminescence imaging system (Vilber,
492 Marne-la-Vallée, France). α-tubulin was used as a loading control. Band intensities were
493 quantified using ImageJ software. Antibodies used in this study were listed in Supplemental
494 Table 1. Primary and secondary antibodies were diluted 1:1000 and 1:10000 with PBS
495 containing 0.1% Tween-20 and 3% BSA, respectively.

496

497 **FAPs transplantation**

498 YFP$^{+}$ or tdTomato$^{+}$ FAPs were isolated by FACS from the limb muscles of indicated mice.
499 $1\times10^{5}$ FAPs were suspended in 0.1% gelatin (Sigma Aldrich; St. Louis, MO, USA) in PBS
500 and then transplanted into one side of the TA muscles of SMN2 1-copy Smn$^{\Delta MPC}$ mice. The
501 contralateral muscle received an equivalent volume of 0.1% gelatin in PBS (Vehicle).

502

503 **Electrophysiology**

504 The extensor digitorum longus (EDL) muscle was dissected from control and SMN2 1-copy
505 Smn$^{\Delta MPC}$ mice, along with the peroneal nerve, and then pinned to a Sylgard-coated recording
506 chamber. Intracellular recording was conducted in oxygenated Ringer's solution, which
507 comprised 138.8 mM NaCl, 4 mM KCl, 12 mM NaHCO3, 1 mM KH2PO4, 1 mM MgCl2
508 and 2 mM CaCl2 with a pH of 7.4. Action potential of the muscle was prevented by preparing
509 the muscle in 2.5 uM μ-conotoxin GIIB (Alomone, Jerusalem, Israel) for 10 minutes
510 beforehand. The recording was performed in toxin-free Ringer's solution. Miniature endplate
511 potentials (mEPPs) were recorded from a junction, followed by recordings of evoked
512 endplate potentials (eEPPs) by stimulating the attached peroneal nerve. The eEPPs were
513 elicited using evoked stimulation. Paired-pulse stimulation (10 ms inter-stimulus interval)
514 was utilized to assess synaptic transmission. The data was obtained and analyzed with
515 Axoclamp 900A and Clampfit version 10.7 software.

516

517 **Transmission electron microscopy**

518 NMJ transmission electron microscopy followed a modified protocol previously reported
519 (Modla et al., 2010). Mouse EDL muscle was swiftly excised and fixed in 4%
520 paraformaldehyde (PFA) dissolved in Sorensen's phosphate buffer (0.1M, pH 7.2), followed
521 by washing in 0.1 M phosphate buffer. The EDL was then gradually infiltrated on a rotator at
522 room temperature with sucrose: 0.1M phosphate buffer solutions of 30% and 50%, for one
523 hour each, followed by an overnight incubation in 70% sucrose. Excess sucrose was then
524 eliminated using filter paper, and the muscle was embedded in an optimal cutting temperature
525 compound (O.C.T.; Sakura Fineteck, Torrance, CA, USA), followed by being frozen in a
526 cryostat (Leica, Wetzlar, Germany). 10-µm thick longitudinal sections were washed in PBS
527 and treated with Alexa fluor 555-conjugated α-bungarotoxin (1:500, Invitrogen) for an hour.
528 Imaging was conducted with the EVOS M7000 imaging system, and we selected 4-5 NMJ-
529 rich regions for processing with TEM. The sections were fixed with 2% glutaraldehyde and 2%
530 PFA in 0.1M cacodylate buffer (pH 7.2) for two hours at room temperature, with an
531 additional overnight incubation at 4°C. After washing with 0.1M cacodylate buffer they were
532 post-fixed with 1% osmium tetraoxide in 0.1M cacodylate buffer (pH 7.2)- for two hours at
533 4°C. The sections were then stained en bloc with 0.5% uranyl acetate overnight, washed with
534 distilled water, and dehydrated using serial ethanol and propylene oxide. The sections were
535 embedded in epoxy resin (Embed-812, Electron Microscopy Sciences) and detached from the
536 slides by dipping them in liquid nitrogen. Ultra-thin sections (70nm) were prepared with a
537 diamond knife on an ultramicrotome (ULTRACUT UC7, Leica) and mounted on 100 mesh
538 copper grids. Sections were stained with 2% uranyl acetate for 10 minutes and lead citrate for
539 3 minutes, then observed using a transmission electron microscope (80kV, JEM1010, JEOL
540 or 120kV, Talos L120C, FEI). Synaptic vesicle density was quantified within a distance of
541 500 nm from the presynaptic membrane.

542

543 **Immunohistochemistry**

544 Freshly dissected TA muscles were fixed in 4% PFA for 30 min at room temperature.
545 Subsequently, the muscles were cryoprotected in 30% sucrose overnight, embedded in O.C.T.,
546 snap-frozen in liquid nitrogen, and stored at -80°C prior to sectioning. Longitudinal 40 μm-
547 thick sections were obtained from the embedded muscles using a cryostat. The sections were
548 blocked for 2 hours at room temperature using 5% goat serum and 5% bovine serum albumin
549 in PBS/0.4% Triton X-100. Then, the sections were incubated with primary antibodies in the
550 blocking buffer for two days at 4 °C. After washing the sections three times with PBS/0.4%
551 Triton X-100, the sections were stained with secondary antibodies overnight at 4 °C, and then
552 incubated with Alexa fluor 488 or 555-conjugated α-bungarotoxin (1:500, Invitrogen) for 2hr
553 at RT, washed three times with PBS/0.4% Triton X-100 and mounted in VECTASHIELD. Z-
554 serial images were collected at 40X with a Leica SP8 confocal laser scanning microscope. To
555 analyze NMJ morphology, LasX software was used to obtain maximal projections.
556 Neurofilament (NF) varicosity refers to the varicose NF end connected to the rest of the nerve
557 terminal. To quantify NMJ size and synaptophysin coverage, the Btx area and synaptophysin
558 area were measured by ImageJ analysis software.

559

560 **Statistical analysis**

561 All statistical analyses were performed using GraphPad Prism 9 (GraphPad Software). For
562 comparison of significant differences in multiple groups for normally distributed data,
563 statistical analysis was performed by one-way or two-way ANOVA followed by Tukey's

pairwise comparison post hoc test. For non-normally distributed data, Brown–Forsythe and Welch ANOVA followed by Games-Howell multiple comparisons test was used. For the comparison of two groups, Student's unpaired t-test assuming a two-tailed distribution with Welch's correction was used. Unless otherwise noted, all error bars represent s.e.m. The number of biological replicates and statistical analyses for each experiment were indicated in the figure legends. Independent experiments were performed at least in triplicates. $P < 0.05$ was considered statistically significant at the 95% confidence level. $*p < 0.05$, $**p < 0.01$, $***p < 0.001$, $****p < 0.0001$.

**Supplemental information**

Supplemental information includes one Supplementary Table.

**Ethics**

The care and treatment of animals were approved by the IACUC of Seoul National University.

**Acknowledgments**

We express our gratitude to the Kong and Choi laboratory members for their valuable feedback during the project. This work was supported by the National Research Foundation of Korea (NRF-2022R1A2C3007621 and NRF-2020R1A5A1018081).

585 **References**


586 Bachman, J. F., & Chakkalakal, J. V. (2022). Insights into muscle stem cell dynamics during
587 postnatal development. *FEBS Journal*, *289*(10), 2710–2722.
588 https://doi.org/10.1111/febs.15856

589 Baranello, G., Vai, S., Broggi, F., Masson, R., Arnoldi, M. T., Zanin, R., Mastella, C., &
590 Bianchi, M. L. (2019). Evolution of bone mineral density, bone metabolism and fragility
591 fractures in Spinal Muscular Atrophy (SMA) types 2 and 3. *Neuromuscular Disorders*,
592 *29*(7), 525–532. https://doi.org/10.1016/j.nmd.2019.06.001

593 Besse, A., Astord, S., Marais, T., Roda, M., Giroux, B., Lejeune, F. X., Relaix, F., Smeriglio,
594 P., Barkats, M., & Biferi, M. G. (2020). AAV9-Mediated Expression of SMN Restricted
595 to Neurons Does Not Rescue the Spinal Muscular Atrophy Phenotype in Mice.
596 *Molecular Therapy*, *28*(8), 1887–1901. https://doi.org/10.1016/j.ymthe.2020.05.011

597 Bosch-Marcé, M., Wee, C. D., Martinez, T. L., Lipkes, C. E., Choe, D. W., Kong, L., Van
598 Meerbeke, J. P., Musarò, A., & Sumner, C. J. (2011). Increased IGF-1 in muscle
599 modulates the phenotype of severe SMA mice. Human Molecular Genetics, 20(9),
600 1844–1853. https://doi.org/10.1093/hmg/ddr067

601 Camps, J., Breuls, N., Sifrim, A., Giarratana, N., Corvelyn, M., Danti, L., Grosemans, H.,
602 Vanuytven, S., Thiry, I., Belicchi, M., Meregalli, M., Platko, K., MacDonald, M. E.,
603 Austin, R. C., Gijsbers, R., Cossu, G., Torrente, Y., Voet, T., & Sampaolesi, M. (2020).
604 Interstitial Cell Remodeling Promotes Aberrant Adipogenesis in Dystrophic Muscles.
605 *Cell Reports*, *31*(5), 107597. https://doi.org/10.1016/j.celrep.2020.107597

606 Cifuentes-Diaz, C., Frugier, T., Tiziano, F. D., Lacène, E., Roblot, N., Joshi, V., Moreau, M.
607 H., & Melki, J. (2001). Deletion of murine SMN exon 7 directed to skeletal muscle leads
608 to severe muscular dystrophy. Journal of Cell Biology, 152(5), 1107–1114.
609 https://doi.org/10.1083/jcb.152.5.1107

610 Claborn, M. K., Stevens, D. L., Walker, C. K., & Gildon, B. L. (2019). Nusinersen: A
611 Treatment for Spinal Muscular Atrophy. *Annals of Pharmacotherapy*, *53*(1), 61–69.
612 https://doi.org/10.1177/1060028018789956

613 Colella, P., Ronzitti, G., & Mingozzi, F. (2018). Emerging Issues in AAV-Mediated In Vivo
614 Gene Therapy. *Molecular Therapy - Methods and Clinical Development*, *8*(March), 87–
615 104. https://doi.org/10.1016/j.omtm.2017.11.007

616 Contreras, O., Rossi, F. M. V., & Theret, M. (2021). Origins, potency, and heterogeneity of
617 skeletal muscle fibro-adipogenic progenitors—time for new definitions. *Skeletal Muscle*,
618 *11*(1), 1–25. https://doi.org/10.1186/s13395-021-00265-6

619 Currie, J. D., Grosser, L., Murawala, P., Schuez, M., Michel, M., Tanaka, E. M., & Sandoval-
620 Guzman, T. (2019). The Prrx1 limb enhancer marks an adult subpopulation of injury-

621 responsive dermal fibroblasts. *Biology Open*, *8*(7), 1–25.
622 https://doi.org/10.1242/bio.043711

623 Dale, J. M., Shen, H., Barry, D. M., Garcia, V. B., Rose, F. F., Lorson, C. L., & Garcia, M. L.
624 (2011). The spinal muscular atrophy mouse model, SMAΔ7, displays altered axonal
625 transport without global neurofilament alterations. Acta Neuropathologica, 122(3), 331–
626 341. https://doi.org/10.1007/s00401-011-0848-5

627 Deguise, M., Pileggi, C., Repentigny, Y. De, Beauvais, A., Tierney, A., Chehade, L.,
628 Michaud, J., Llavero-hurtado, M., Lamont, D., Atrih, A., Wishart, T. M., Gillingwater, T.
629 H., Schneider, B. L., Harper, M., Parson, S. H., & Kothary, R. (2021). SMN Depleted
630 Mice Offer a Robust and Rapid Onset Model of. *Cellular and Molecular*
631 *Gastroenterology and Hepatology*, *12*(1), 354-377.e3.
632 https://doi.org/10.1016/j.jcmgh.2021.01.019

633 Deschenes, M. R., Tenny, K. A., & Wilson, M. H. (2006). Increased and decreased activity
634 elicits specific morphological adaptations of the neuromuscular junction. *Neuroscience*,
635 *137*(4), 1277–1283. https://doi.org/10.1016/j.neuroscience.2005.10.042

636 Foust, K. D., Nurre, E., Montgomery, C. L., Hernandez, A., Chan, C. M., & Kaspar, B. K.
637 (2009). Intravascular AAV9 preferentially targets neonatal neurons and adult astrocytes.
638 *Nature Biotechnology*, *27*(1), 59–65. https://doi.org/10.1038/nbt.1515

639 Foust, K. D., Wang, X., McGovern, V. L., Braun, L., Bevan, A. K., Haidet, A. M., Le, T. T.,
640 Morales, P. R., Rich, M. M., Burghes, A. H. M., & Kaspar, B. K. (2022). Retraction
641 Note: Rescue of the spinal muscular atrophy phenotype in a mouse model by early
642 postnatal delivery of SMN. *Nature Biotechnology*, *40*(11), 1692–1692.
643 https://doi.org/10.1038/s41587-022-01497-7

644 Frugier, T., Tiziano, F. D., Cifuentes-Diaz, C., Miniou, P., Roblot, N., Dierich, A., Le Meur,
645 M., & Melki, J. (2000). Nuclear targeting defect of SMN lacking the C-terminus in a
646 mouse model of spinal muscular atrophy. *Human Molecular Genetics*, *9*(5), 849–858.
647 https://doi.org/10.1093/hmg/9.5.849

648 Heller, G. J., Marshall, M. S., Issa, Y., Marshall, J. N., Nguyen, D., Rue, E., Pathmasiri, K. C.,
649 Domowicz, M. S., van Breemen, R. B., Tai, L. M., Cologna, S. M., Crocker, S. J.,
650 Givogri, M. I., Sands, M. S., & Bongarzone, E. R. (2021). Waning efficacy in a long-
651 term AAV-mediated gene therapy study in the murine model of Krabbe disease.
652 *Molecular Therapy*, *29*(5), 1883–1902. https://doi.org/10.1016/j.ymthe.2021.01.026

653 Hensel, N., Brickwedde, H., Tsaknakis, K., Grages, A., Braunschweig, L., Lüders, K. A.,
654 Lorenz, H. M., Lippross, S., Walter, L. M., Tavassol, F., Lienenklaus, S., Neunaber, C.,
655 Claus, P., & Hell, A. K. (2020). Altered bone development with impaired cartilage
656 formation precedes neuromuscular symptoms in spinal muscular atrophy. *Human*
657 *Molecular Genetics*, *29*(16), 2662–2673. https://doi.org/10.1093/hmg/ddaa145

658 Hoxha, R., Islami, H., QorrajBytyqi, H., Thaci, S., & Bahtiri, E. (2014). Relationship of
659 Weight and Body Mass Index with Bone Mineral Density in Adult Men from Kosovo.
660 *Materia Socio Medica*, *26*(5), 306. https://doi.org/10.5455/msm.2014.26.306-308

661 Hua, Y., Sahashi, K., Rigo, F., Hung, G., Horev, G., Bennett, C. F., & Krainer, A. R. (2011).
662 Peripheral SMN restoration is essential for long-term rescue of a severe spinal muscular
663 atrophy mouse model. *Nature*, *478*(7367), 123–126. https://doi.org/10.1038/nature10485

664 Passini, M. A., Bu, J., Roskelley, E. M., Richards, A. M., Sardi, S. P., O'Riordan, C. R.,
665 Klinger, K. W., Shihabuddin, L. S., & Cheng, S. H. (2010). CNS-targeted gene therapy
666 improves survival and motor function in a mouse model of spinal muscular atrophy.
667 Journal of Clinical Investigation, 120(4), 1253–1264. https://doi.org/10.1172/JCI41615

668 Torres-Benito, L., Neher, M. F., Cano, R., Ruiz, R., & Tabares, L. (2011). SMN requirement
669 for synaptic vesicle, active zone and microtubule postnatal organization in motor nerve
670 terminals. PLoS ONE, 6(10). https://doi.org/10.1371/journal.pone.0026164

671 Ike, H., Inaba, Y., Kobayashi, N., Hirata, Y., Yukizawa, Y., Aoki, C., Choe, H., & Saito, T.
672 (2015). Comparison between mechanical stress and bone mineral density in the femur
673 after total hip arthroplasty by using subject-specific finite element analyses. *Computer*
674 *Methods in Biomechanics and Biomedical Engineering*, *18*(10), 1056–1065.
675 https://doi.org/10.1080/10255842.2013.869320

676 Jonason, J. H., Hoak, D., & O'Keefe, R. J. (2015). Primary Murine Growth Plate and
677 Articular Chondrocyte Isolation and Cell Culture. In *Osteoporosis and Osteoarthritis*
678 (Vol. 1226, pp. 11–18). https://doi.org/10.1007/978-1-4939-1619-1_2

679 Kariya, S., Park, G. H., Maeno-Hikichi, Y., Leykekhman, O., Lutz, C., Arkovitz, M. S.,
680 Landmesser, L. T., & Monani, U. R. (2008). Reduced SMN protein impairs maturation
681 of the neuromuscular junctions in mouse models of spinal muscular atrophy. *Human*
682 *Molecular Genetics*, *17*(16), 2552–2569. https://doi.org/10.1093/hmg/ddn156

683 Kariya, S., Obis, T., Garone, C., Akay, T., Sera, F., Iwata, S., Homma, S., & Monani, U. R.
684 (2014). Requirement of enhanced Survival Motoneuron protein imposed during
685 neuromuscular junction maturation. Journal of Clinical Investigation, 124(2), 785–800.
686 https://doi.org/10.1172/JCI72017

687 Khatri, I. A., Chaudhry, U. S., Seikaly, M. G., Browne, R. H., & Iannaccone, S. T. (2008).
688 Low bone mineral density in spinal muscular atrophy. *Journal of Clinical*
689 *Neuromuscular Disease*, *10*(1), 11–17. https://doi.org/10.1097/CND.0b013e318183e0fa

690 Kim, J. K., Jha, N. N., Feng, Z., Faleiro, M. R., Chiriboga, C. A., Wei-Lapierre, L., Dirksen,
691 R. T., Ko, C. P., & Monani, U. R. (2020). Muscle-specific SMN reduction reveals motor
692 neuron–independent disease in spinal muscular atrophy models. Journal of Clinical
693 Investigation, 130(3), 1271–1287. https://doi.org/10.1172/JCI131989

694 Kim, J. H., Kang, J. S., Yoo, K., Jeong, J., Park, I., Park, J. H., Rhee, J., Jeon, S., Jo, Y. W.,
695 Hann, S. H., Seo, M., Moon, S., Um, S. J., Seong, R. H., & Kong, Y. Y. (2022).
696 Bap1/SMN axis in Dpp4+ skeletal muscle mesenchymal cells regulates the
697 neuromuscular system. *JCI Insight*, *7*(10). https://doi.org/10.1172/jci.insight.158380

698 Kong, L., Wang, X., Choe, D. W., Polley, M., Burnett, B. G., Bosch-Marcé, M., Griffin, J.
699 W., Rich, M. M., & Sumner, C. J. (2009). Impaired synaptic vesicle release and
700 immaturity of neuromuscular junctions in spinal muscular atrophy mice. *Journal of*
701 *Neuroscience*, *29*(3), 842–851. https://doi.org/10.1523/JNEUROSCI.4434-08.2009

702 Leinroth, A. P., Mirando, A. J., Rouse, D., Kobayahsi, Y., Tata, P. R., Rueckert, H. E., Liao,
703 Y., Long, J. T., Chakkalakal, J. V., & Hilton, M. J. (2022). Identification of distinct non-
704 myogenic skeletal-muscle-resident mesenchymal cell populations. *Cell Reports*, *39*(6),
705 110785. https://doi.org/10.1016/j.celrep.2022.110785

706 Ling, K. K. Y., Lin, M. Y., Zingg, B., Feng, Z., & Ko, C. P. (2010). Synaptic defects in the
707 spinal and neuromuscular circuitry in a mouse model of spinal muscular atrophy. *PLoS*
708 *ONE*, *5*(11). https://doi.org/10.1371/journal.pone.0015457

709 Martinez, T. L., Kong, L., Wang, X., Osborne, M. A., Crowder, M. E., Van Meerbeke, J. P.,
710 Xu, X., Davis, C., Wooley, J., Goldhamer, D. J., Lutz, C. M., Rich, M. M., & Sumner, C.
711 J. (2012). Survival Motor Neuron Protein in Motor Neurons Determines Synaptic
712 Integrity in Spinal Muscular Atrophy. *Journal of Neuroscience*, *32*(25), 8703–8715.
713 https://doi.org/10.1523/JNEUROSCI.0204-12.2012

714 Mattar, C. N., Waddington, S. N., Biswas, A., Johana, N., Ng, X. W., Fisk, A. S., Fisk, N. M.,
715 Tan, L. G., Rahim, A. A., Buckley, S. M. K., Tan, M. H., Lu, J., Choolani, M., & Chan,
716 J. K. Y. (2013). Systemic delivery of scAAV9 in fetal macaques facilitates neuronal
717 transduction of the central and peripheral nervous systems. *Gene Therapy*, *20*(1), 69–83.
718 https://doi.org/10.1038/gt.2011.216

719 McGovern, V. L., Iyer, C. C., David Arnold, W., Gombash, S. E., Zaworski, P. G., Blatnik, A.
720 J., Foust, K. D., & Burghes, A. H. M. (2015). SMN expression is required in motor
721 neurons to rescue electrophysiological deficits in the SMNΔ7 mouse model of SMA.
722 *Human Molecular Genetics*, *24*(19), 5524–5541. https://doi.org/10.1093/hmg/ddv283

723 Mercuri, E., Pera, M. C., Scoto, M., Finkel, R., & Muntoni, F. (2020). Spinal muscular
724 atrophy — insights and challenges in the treatment era. *Nature Reviews Neurology*,
725 *16*(12), 706–715. https://doi.org/10.1038/s41582-020-00413-4

726 Modla, S., Mendonca, J., Czymmek, K. J., & Akins, R. E. (2010). Identification of
727 neuromuscular junctions by correlative confocal and transmission electron microscopy.
728 *Journal of Neuroscience Methods*, *191*(2), 158–165.
729 https://doi.org/10.1016/j.jneumeth.2010.06.015

730 Monani, U. R., Pastore, M. T., Gavrilina, T. O., Jablonka, S., Le, T. T., Andreassi, C.,
731 DiCocco, J. M., Lorson, C., Androphy, E. J., Sendtner, M., Podell, M., & Burghes, A. H.

732 M. (2003). A transgene carrying an A2G missense mutation in the SMN gene modulates
733 phenotypic severity in mice with severe (type I) spinal muscular atrophy. *Journal of Cell*
734 *Biology*, *160*(1), 41–52. https://doi.org/10.1083/jcb.200208079

735 Monani, U. R., Sendtner, M., Coovert, D. D., Parsons, D. W., Andreassi, C., Le, T. T.,
736 Jablonka, S., Schrank, B., Rossol, W., Prior, T. W., Morris, G. E., & Burghes, A. H. M.
737 (2000). The human centromeric survival motor neuron gene (SMN2) rescues embryonic
738 lethality in Smn(-/-) mice and results in a mouse with spinal muscular atrophy. *Human*
739 *Molecular Genetics*, *9*(3), 333–339. https://doi.org/10.1093/hmg/9.3.333

740 Nassari, S., Duprez, D., & Fournier-Thibault, C. (2017). Non-myogenic Contribution to
741 Muscle Development and Homeostasis: The Role of Connective Tissues. *Frontiers in*
742 *Cell and Developmental Biology*, *5*(March), 1–17.
743 https://doi.org/10.3389/fcell.2017.00022

744 Ovchinnikov, D. (2009). Alcian blue/alizarin red staining of cartilage and bone in mouse.
745 *Cold Spring Harbor Protocols*, *4*(3), 5170–5172. https://doi.org/10.1101/pdb.prot5170

746 Passini, M. A., Bu, J., Roskelley, E. M., Richards, A. M., Sardi, S. P., O'Riordan, C. R.,
747 Klinger, K. W., Shihabuddin, L. S., & Cheng, S. H. (2010). CNS-targeted gene therapy
748 improves survival and motor function in a mouse model of spinal muscular atrophy.
749 Journal of Clinical Investigation, 120(4), 1253–1264. https://doi.org/10.1172/JCI41615

750 Passini, M. A., Bu, J., Richards, A. M., Kinnecom, C., Sardi, S. P., Stanek, L. M., Hua, Y.,
751 Rigo, F., Matson, J., Hung, G., Kaye, E. M., Shihabuddin, L. S., Krainer, A. R., Bennett,
752 C. F., & Cheng, S. H. (2011). Antisense oligonucleotides delivered to the mouse CNS
753 ameliorate symptoms of severe spinal muscular atrophy. *Science Translational Medicine*,
754 *3*(72), 1–12. https://doi.org/10.1126/scitranslmed.3001777

755 Penaud-Budloo, M., Le Guiner, C., Nowrouzi, A., Toromanoff, A., Chérel, Y., Chenuaud, P.,
756 Schmidt, M., von Kalle, C., Rolling, F., Moullier, P., & Snyder, R. O. (2008). Adeno-
757 Associated Virus Vector Genomes Persist as Episomal Chromatin in Primate Muscle.
758 *Journal of Virology*, *82*(16), 7875–7885. https://doi.org/10.1128/jvi.00649-08

759 Petrany, M. J., Swoboda, C. O., Sun, C., Chetal, K., Chen, X., Weirauch, M. T., Salomonis,
760 N., & Millay, D. P. (2020). Single-nucleus RNA-seq identifies transcriptional
761 heterogeneity in multinucleated skeletal myofibers. *Nature Communications*, *11*(1).
762 https://doi.org/10.1038/s41467-020-20063-w

763 Ross, J. A., Webster, R. G., Lechertier, T., Reynolds, L. E., Turmaine, M., Bencze, M.,
764 Jamshidi, Y., Cetin, H., Muntoni, F., Beeson, D., Hodilvala-Dilke, K., & Conti, F. J.
765 (2017). Multiple roles of integrin-α3 at the neuromuscular junction. Journal of Cell
766 Science, 130(10), 1772–1784. https://doi.org/10.1242/jcs.201103

767 Sahashi, K., Ling, K. K. Y., Hua, Y., Wilkinson, J. E., Nomakuchi, T., Rigo, F., Hung, G.,
768 Xu, D., Jiang, Y. P., Lin, R. Z., Ko, C. P., Bennett, C. F., & Krainer, A. R. (2013).

769 Pathological impact of SMN2 mis-splicing in adult SMA mice. *EMBO Molecular*
770 *Medicine*, *5*(10), 1586–1601. https://doi.org/10.1002/emmm.201302567

771 Scott, R. W., Arostegui, M., Schweitzer, R., Rossi, F. M. V., & Underhill, T. M. (2019). Hic1
772 Defines Quiescent Mesenchymal Progenitor Subpopulations with Distinct Functions and
773 Fates in Skeletal Muscle Regeneration. *Cell Stem Cell*, *25*(6), 797-813.e9.
774 https://doi.org/10.1016/j.stem.2019.11.004

775 Shababi, M., Lorson, C. L., & Rudnik-Schöneborn, S. S. (2014). Spinal muscular atrophy: A
776 motor neuron disorder or a multi-organ disease? *Journal of Anatomy*, *224*(1), 15–28.
777 https://doi.org/10.1111/joa.12083

778 Sheng, G. (2015). The developmental basis of mesenchymal stem/stromal cells (MSCs).
779 *BMC Developmental Biology*, *15*(1), 26–31. https://doi.org/10.1186/s12861-015-0094-5

780 Torres-Benito, L., Neher, M. F., Cano, R., Ruiz, R., & Tabares, L. (2011). SMN requirement
781 for synaptic vesicle, active zone and microtubule postnatal organization in motor nerve
782 terminals. PLoS ONE, 6(10). https://doi.org/10.1371/journal.pone.0026164

783 Tsai, L. K., Chen, C. L., Ting, C. H., Lin-Chao, S., Hwu, W. L., Dodge, J. C., Passini, M. A.,
784 & Cheng, S. H. (2014). Systemic administration of a recombinant AAV1 vector
785 encoding IGF-1 improves disease manifestations in SMA mice. Molecular Therapy,
786 22(8), 1450–1459. https://doi.org/10.1038/mt.2014.84

787 Uezumi, A., Ikemoto-Uezumi, M., Zhou, H., Kurosawa, T., Yoshimoto, Y., Nakatani, M.,
788 Hitachi, K., Yamaguchi, H., Wakatsuki, S., Araki, T., Morita, M., Yamada, H., Toyoda,
789 M., Kanazawa, N., Nakazawa, T., Hino, J., Fukada, S. I., & Tsuchida, K. (2021).
790 Mesenchymal Bmp3b expression maintains skeletal muscle integrity and decreases in
791 age-related sarcopenia. *Journal of Clinical Investigation*, *131*(1).
792 https://doi.org/10.1172/JCI139617

793 Vai, S., Bianchi, M. L., Moroni, I., Mastella, C., Broggi, F., Morandi, L., Arnoldi, M. T.,
794 Bussolino, C., & Baranello, G. (2015). Bone and Spinal Muscular Atrophy. *Bone*, *79*,
795 116–120. https://doi.org/10.1016/j.bone.2015.05.039

796 Valori, C. F., Ning, K., Wyles, M., Mead, R. J., Grierson, A. J., Shaw, P. J., & Azzouz, M.
797 (2010). Systemic delivery of scAAV9 expressing SMN prolongs survival in a model of
798 spinal muscular atrophy. *Science Translational Medicine*, *2*(35), 1–9.
799 https://doi.org/10.1126/scitranslmed.3000830

800 Van Alstyne, M., Tattoli, I., Delestrée, N., Recinos, Y., Workman, E., Shihabuddin, L. S.,
801 Zhang, C., Mentis, G. Z., & Pellizzoni, L. (2021). Gain of toxic function by long-term
802 AAV9-mediated SMN overexpression in the sensorimotor circuit. *Nature Neuroscience*.
803 https://doi.org/10.1038/s41593-021-00827-3

804 Wasserman, H. M., Hornung, L. N., Stenger, P. J., Rutter, M. M., Wong, B. L., Rybalsky, I.,
805 Khoury, J. C., & Kalkwarf, H. J. (2017). Low bone mineral density and fractures are

806 highly prevalent in pediatric patients with spinal muscular atrophy regardless of disease
807 severity. *Neuromuscular Disorders*, *27*(4), 331–337.
808 https://doi.org/10.1016/j.nmd.2017.01.019

809 Wilk, K., Yeh, S. C. A., Mortensen, L. J., Ghaffarigarakani, S., Lombardo, C. M., Bassir, S.
810 H., Aldawood, Z. A., Lin, C. P., & Intini, G. (2017). Postnatal Calvarial Skeletal Stem
811 Cells Expressing PRX1 Reside Exclusively in the Calvarial Sutures and Are Required
812 for Bone Regeneration. *Stem Cell Reports*, *8*(4), 933–946.
813 https://doi.org/10.1016/j.stemcr.2017.03.002

814 Wosczyna, M. N., Konishi, C. T., Perez Carbajal, E. E., Wang, T. T., Walsh, R. A., Gan, Q.,
815 Wagner, M. W., & Rando, T. A. (2019). Mesenchymal Stromal Cells Are Required for
816 Regeneration and Homeostatic Maintenance of Skeletal Muscle. *Cell Reports*, *27*(7),
817 2029-2035.e5. https://doi.org/10.1016/j.celrep.2019.04.074

818 Yakar, S., Rosen, C. J., Beamer, W. G., Ackert-Bicknell, C. L., Wu, Y., Liu, J. L., Ooi, G. T.,
819 Setser, J., Frystyk, J., Boisclair, Y. R., & LeRoith, D. (2002). Circulating levels of IGF-1
820 directly regulate bone growth and density. *Journal of Clinical Investigation*, *110*(6),
821 771–781. https://doi.org/10.1172/JCI0215463

822 Yakar, S., Rosen, C. J., Bouxsein, M. L., Sun, H., Mejia, W., Kawashima, Y., Wu, Y.,
823 Emerton, K., Williams, V., Jepsen, K., Schaffler, M. B., Majeska, R. J., Gavrilova, O.,
824 Gutierrez, M., Hwang, D., Pennisi, P., Frystyk, J., Boisclair, Y., Pintar, J., … LeRoith, D.
825 (2009). Serum complexes of insulin-like growth factor-1 modulate skeletal integrity and
826 carbohydrate metabolism. *The FASEB Journal*, *23*(3), 709–719.
827 https://doi.org/10.1096/fj.08-118976

828 Yang, Y. S., Xie, J., Wang, D., Kim, J. M., Tai, P. W. L., Gravallese, E., Gao, G., & Shim, J.
829 H. (2019). Bone-targeting AAV-mediated silencing of Schnurri-3 prevents bone loss in
830 osteoporosis. *Nature Communications*, *10*(1), 1–13. https://doi.org/10.1038/s41467-019-
831 10809-6

832 Yeo, C. J. J., & Darras, B. T. (2020). Overturning the Paradigm of Spinal Muscular Atrophy
833 as Just a Motor Neuron Disease. *Pediatric Neurology*, *109*, 12–19.
834 https://doi.org/10.1016/j.pediatrneurol.2020.01.003

835 Yesbek Kaymaz, A., Bal, A., Bora-Tatar, G., Ozon, A., Alikasifoglu, A., Topaloglu, H., &
836 Erdem-Yurter, H. (2016). Serum IGF1 and IGFBP3 levels in SMA patients.
837 *Neuromuscular Disorders*, *26*, S105. https://doi.org/10.1016/j.nmd.2016.06.075

838 Zanetti, G., Negro, S., Megighian, A., & Pirazzini, M. (2018). Electrophysiological
839 Recordings of Evoked End-Plate Potential on Murine Neuro-muscular Synapse
840 Preparations. *Bio-Protocol*, *8*(8), 1–16. https://doi.org/10.21769/bioprotoc.2803

841

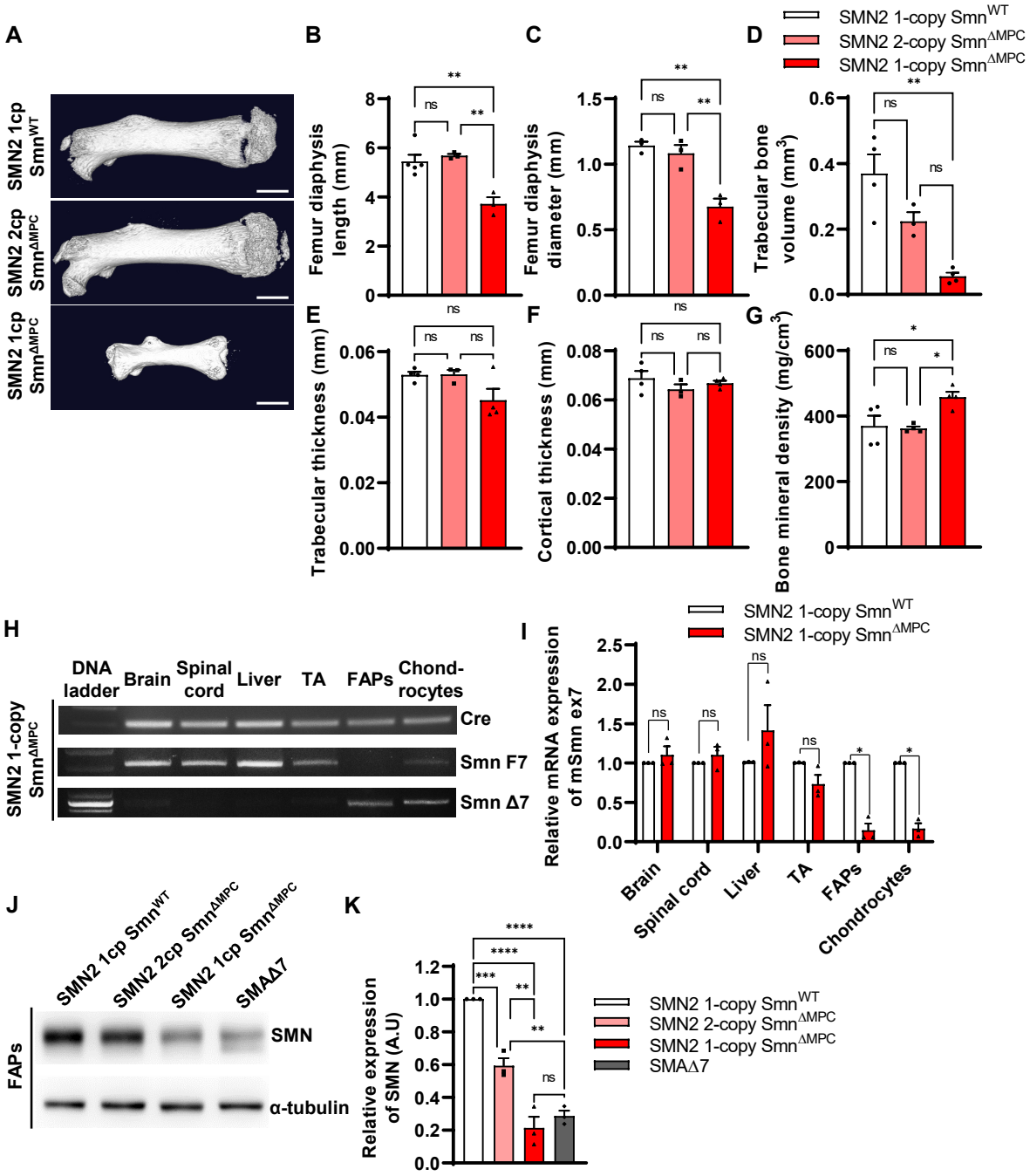
A
SMN2 1cp Smn^WT
SMN2 2cp Smn^ΔMPC
SMN2 1cp Smn^ΔMPC
B
Femur diaphysis length (mm)
C
Femur diaphysis diameter (mm)
D
Trabecular bone volume (mm³)
SMN2 1-copy Smn^WT
SMN2 2-copy Smn^ΔMPC
SMN2 1-copy Smn^ΔMPC
E
Trabecular thickness (mm)
F
Cortical thickness (mm)
G
Bone mineral density (mg/cm³)
H
DNA ladder
Brain
Spinal cord
Liver
TA
FAPs
Chond-rocytes
SMN2 1-copy Smn^ΔMPC
Cre
Smn F7
Smn Δ7
I
Relative mRNA expression of mSmn ex7
Brain
Spinal cord
Liver
TA
FAPs
Chondrocytes
J
SMN2 1cp Smn^WT
SMN2 2cp Smn^ΔMPC
SMN2 1cp Smn^ΔMPC
SMAΔ7
FAPs
SMN
α-tubulin
K
Relative expression of SMN (A.U)
SMN2 1-copy Smn^WT
SMN2 2-copy Smn^ΔMPC
SMN2 1-copy Smn^ΔMPC
SMAΔ7

**Figure 1**

Skeletal growth abnormalities by limb mesenchymal cell-specific SMN depletion in SMN2 1-copy $Smn^{\Delta MPC}$ mice. (**A**) Representative 3D images of ossified femur bone. Scale bars, 1 mm. (**B-C**) SMN2 1-copy mutant's femurs showed reduced growth in diaphysis length and diameter, and (**D**) decreased trabecular bone volume. (**E-F**) Trabecular and cortical bone thicknesses were not significantly different between the control and mutant groups. (**G**) Bone mineral density was slightly increased in the diaphysis of SMN2 1-copy $Smn^{\Delta MPC}$ mice. The micro CT analysis was performed in femur diaphysis and metaphysis from SMN2 1-copy $Smn^{\Delta WT}$, SMN2 2-copy, and 1-copy $Smn^{\Delta MPC}$ mice at P14. 1-way ANOVA with Tukey's post hoc test, n = 3-5 mice in each genotype (**B-G**). (**H**) Representative images of genomic PCR analysis from SMN2 1-copy $Smn^{\Delta MPC}$ mice tissues at P21. (**I**) qRT PCR analysis from tissues of SMN2 1-copy $Smn^{WT}$ and $Smn^{\Delta MPC}$ mice at P21 (n = 3 mice in each genotype; Unpaired t-test with Welch's correction). Deletion of Smn exon 7 was detected only in limb mesenchymal cells using genomic PCR (**H**) and mRNA expression (**I**). (**J**) Representative images of western blot analysis in cultured FAPs. SMN protein in FAPs of SMN2 1-copy $Smn^{\Delta MPC}$ mice exhibited a decrease comparable to that observed in the SMAΔ7 mice. (**K**) Relative SMN levels in cultured FAPs of the controls and mutants (n = 3 mice in each genotype; 1-way ANOVA with Tukey's post hoc test). ns; not significantly different. *$p < 0.05$; **$p < 0.01$; ***$p < 0.001$; ****$p < 0.0001$. Error bars show s.e.m.

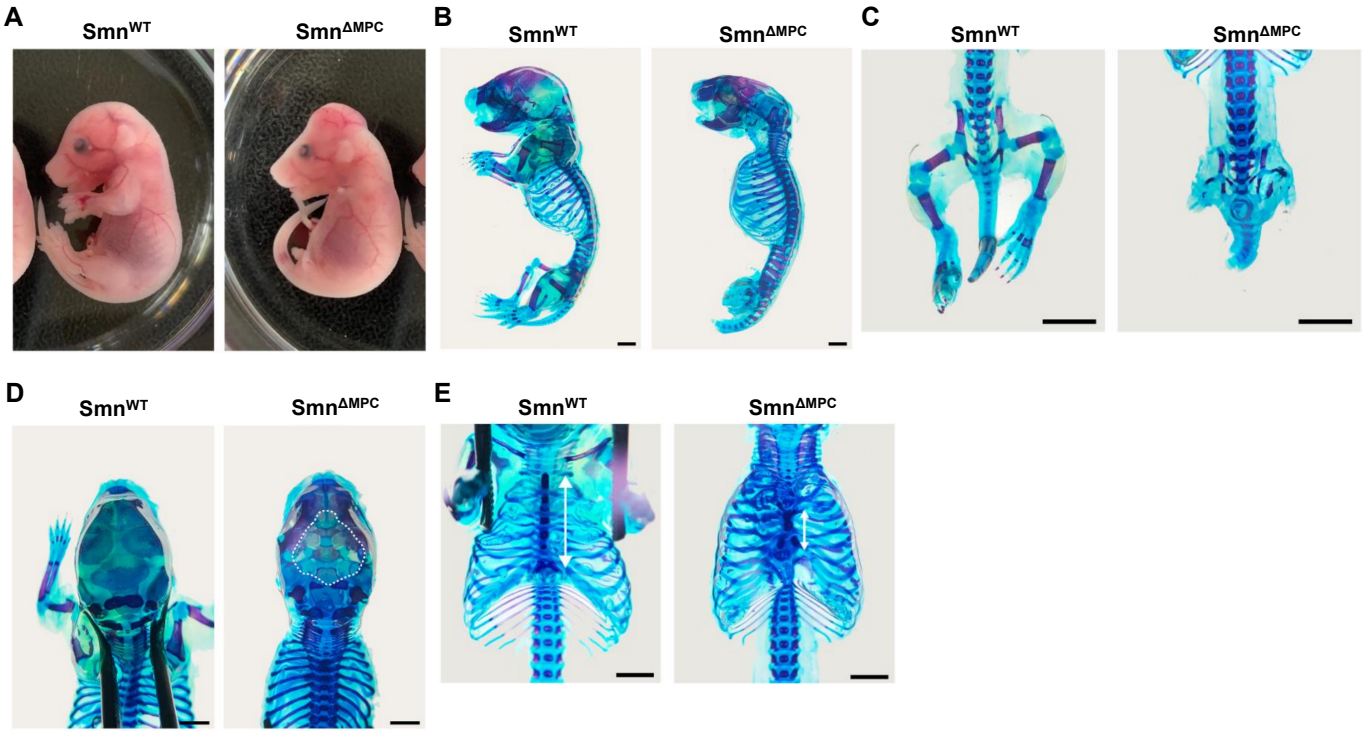
A
Smn^WT
Smn^ΔMPC
B
Smn^WT
Smn^ΔMPC
C
Smn^WT
Smn^ΔMPC
D
Smn^WT
Smn^ΔMPC
E
Smn^WT
Smn^ΔMPC

**Figure 1 -figure supplement 1**

Growth defects in the Prrx1-lineage bone of SMN2 0-copy $Smn^{\Delta MPC}$ mice. (**A)** Representative control and mutant mice with 0 copies of SMN2 were photographed at E18.5. (**B-C**) Alcian blue & alizarine red staining in the SMN2 0-copy $Smn^{\Delta MPC}$ mutant showed abnormal skeletal development of the limbs, (**D**) calvaria (shown by the dashed line), and (**E**) sternum (indicated by a white arrow). Scale bars, 5 mm (**B-C**) and 2 mm (**D-E**).

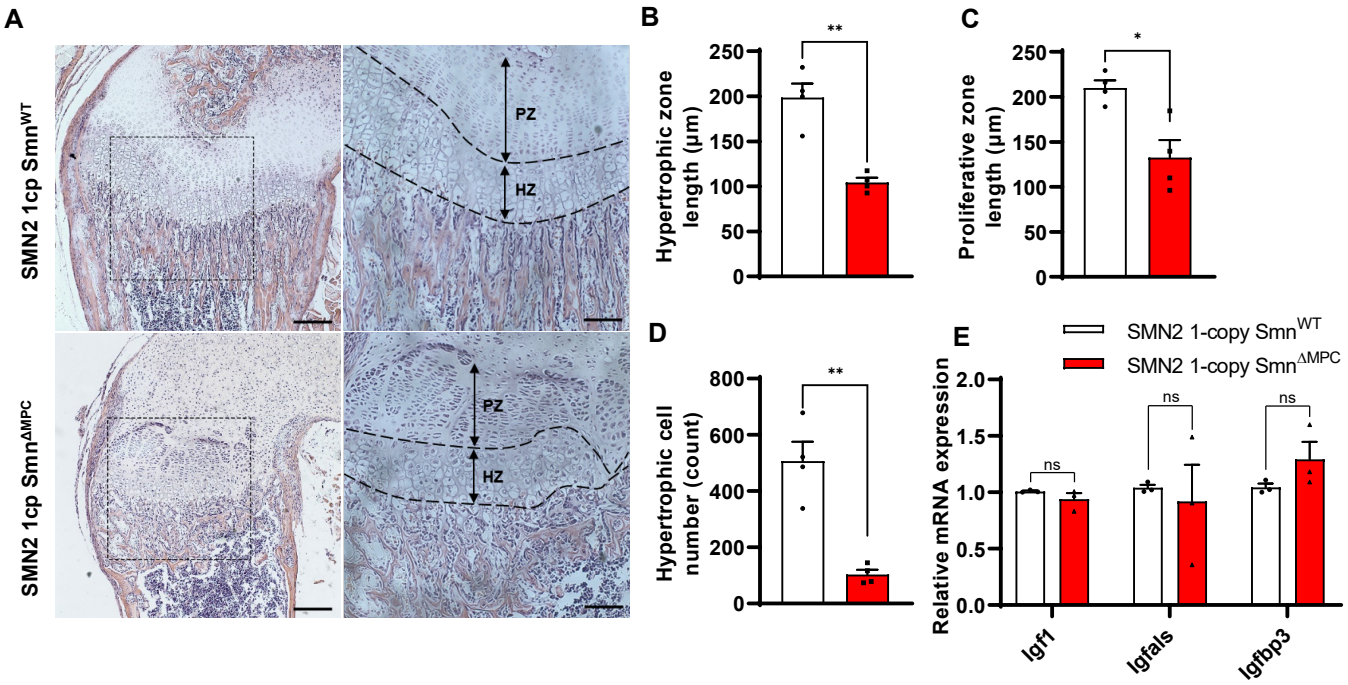
A
SMN2 1cp Smn^WT
SMN2 1cp Smn^ΔMPC
PZ
HZ
PZ
HZ
B
Hypertrophic zone length (µm)
250
200
150
100
50
0
**
C
Proliferative zone length (µm)
250
200
150
100
50
0
*
D
Hypertrophic cell number (count)
800
600
400
200
0
**
E
SMN2 1-copy Smn^WT
SMN2 1-copy Smn^ΔMPC
Relative mRNA expression
2.0
1.5
1.0
0.5
0.0
ns
ns
ns
Igf1
Igfals
Igfbp3

**Figure 1 -figure supplement 2**

Altered growth plate homeostasis independent of the IGF axis from the liver in SMN2 1-copy $Smn^{\Delta MPC}$ mice. (**A)** Representative images of H&E staining in the femur growth plate of control and mutant mice with 1 copy of SMN2 at P14. Scale bars, 200 μm (Left) and 100 μm (Right). (**B-D**) Hypertrophic zone (HZ) and proliferative zone (PZ), indicated by black arrows and dashed lines, lengths were reduced in SMN2 1-copy $Smn^{\Delta MPC}$ mice, and the hypertrophic cell number in a section of the 1-copy mutant was decreased (n = 4 mice in each genotype; Unpaired t-test with Welch's correction). (**E**) Relative IGF axis mRNA expression in the livers of SMN2 1-copy control and mutant mice. The IGF pathway genes showed no difference when comparing controls to SMN2 1-copy $Smn^{\Delta MPC}$ mutants (n = 3 mice in each genotype; Unpaired t-test with Welch's correction). ns; not significantly different. *$p < 0.05$; **$p < 0.01$. Error bars show s.e.m.

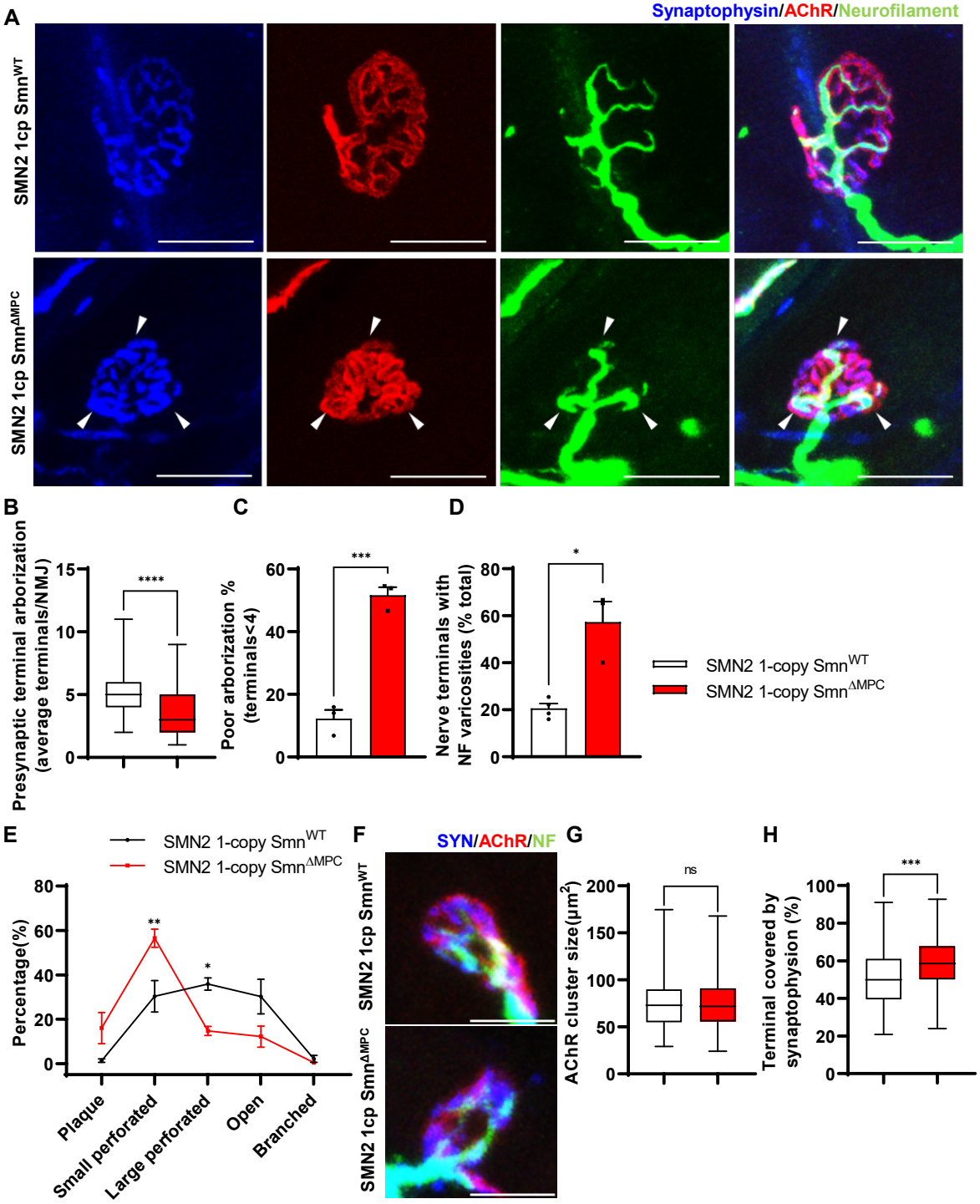
A
Synaptophysin/AChR/Neurofilament
SMN2 1cp Smn^WT
SMN2 1cp Smn^ΔMPC
B
Presynaptic terminal arborization (average terminals/NMJ)
****
C
Poor arborization % (terminals<4)
***
D
Nerve terminals with NF varicosities (% total)
*
SMN2 1-copy Smn^WT
SMN2 1-copy Smn^ΔMPC
E
Percentage(%)
**
*
Plaque
Small perforated
Large perforated
Open
Branched
F
SYN/AChR/NF
G
AChR cluster size(μm²)
ns
H
Terminal covered by synaptophysion (%)
***

**Figure 2**

Aberrant postnatal NMJ maturation in SMN2 1-copy $Smn^{\Delta MPC}$ mice. (**A**) Immunostaining of NMJs in TA muscle of SMN2 1-copy $Smn^{WT}$ and $Smn^{\Delta MPC}$ mice at P21 with anti-NF (Green), anti-synaptophysin (Blue), α-Btx staining AChR (Red). Scale bars, 20 μm. The confocal images of NMJs showed decreased presynaptic terminal branching and the existence of nerve terminal varicosities that were enlarged with NF (indicated by arrowheads) in the mutant. (**B**) The NMJs of the SMN2 1-copy mutant exhibited a significant decrease in presynaptic terminal arborization and (**C**) an increased percentage of poorly arborized NMJs (n = 3 mice in each genotype; Unpaired t-test with Welch's correction). (**D**) The percentage of NMJs exhibiting NF varicosities was higher in the SMN2 1-copy mutant group than in the control group (n = 3-4 mice in each genotype; Unpaired t-test with Welch's correction). (**E**) For quantification of the NMJ maturation stage, we classified NMJs into five distinct developmental stages (Plaque: Plaque-shaped endplate without any perforation; Small perforated: Plaque-shaped endplate with small perforations; Large perforated: Plaque-shaped endplate with large perforations; Open: C-shaped endplate; Branched: Pretzel-like branched -shaped endplate) and then compared the frequency patterns of SMN2 1-copy control and mutant mice (n = 3 mice in each genotype; 2-way ANOVA with Tukey's post hoc test). The NMJs of SMN2 1-copy mutants displayed plaque-like shapes, indicating that they were in the immature stage. (**F**) Immunostaining of NMJs in TA muscle of SMN2 1-copy $Smn^{WT}$ and $Smn^{\Delta MPC}$ mice at P3 with anti-NF (Green), anti-synaptophysin (Blue), α-Btx staining AChR (Red). Scale bars, 10 μm. (**G**) There were no significant differences in AChR cluster size between the SMN2 1-copy control and mutant at P3 (n = 3-4 mice in each genotype; Unpaired t-test with Welch's correction). (**H**) The ratio of the Synaptophysin area to the AChR area in NMJ was slightly higher in the SMN2 1-copy mutant at P3 (n = 3-4 mice in each genotype; Unpaired t-test with

Welch's correction). ns; not significantly different. *$p < 0.05$; **$p < 0.01$; ***$p < 0.001$; ****$p < 0.0001$. All box-and-whisker plots show the median, interquartile range, minimum, and maximum. For the bar and line graph, error bars show s.e.m.

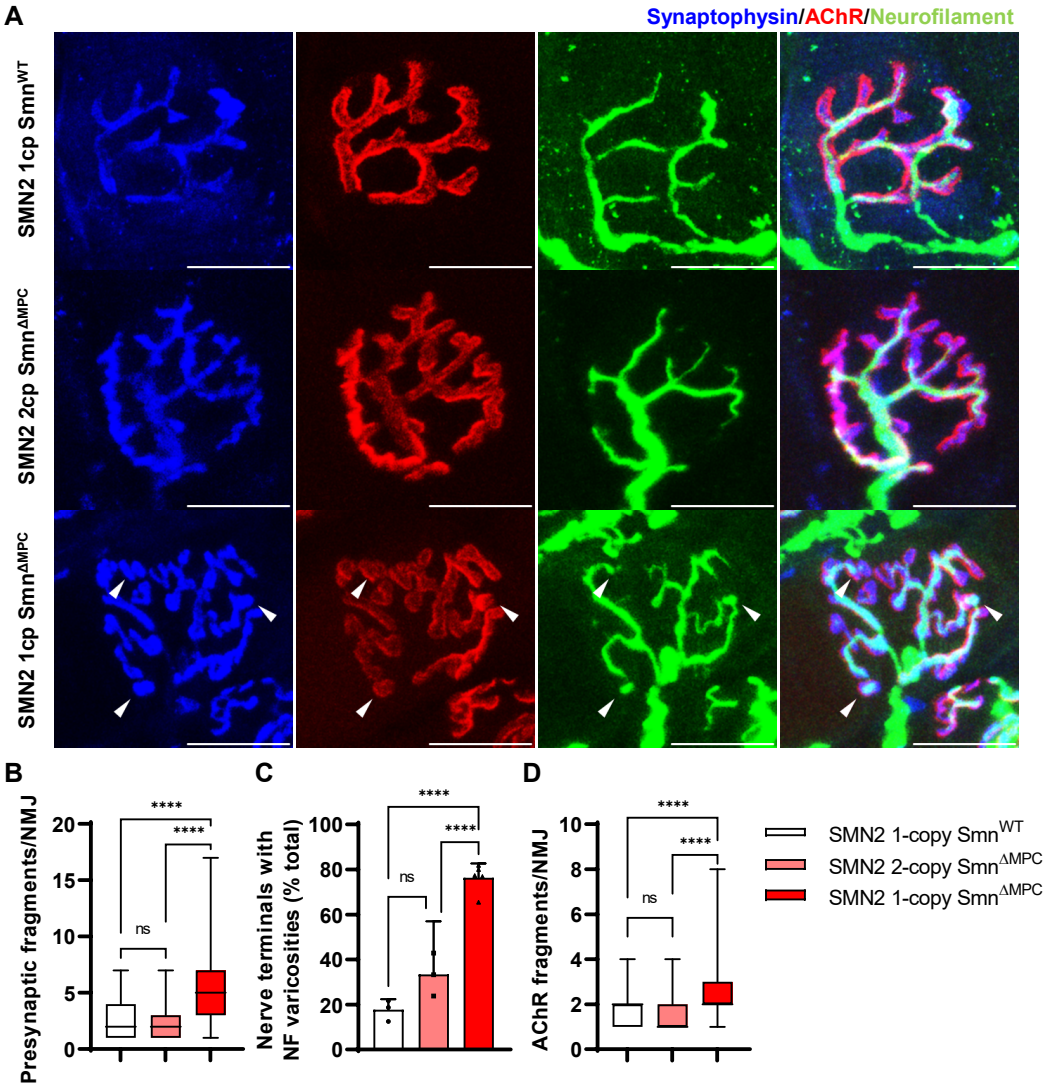
A
Synaptophysin/AChR/Neurofilament
SMN2 1cp Smn^WT
SMN2 2cp Smn^ΔMPC
SMN2 1cp Smn^ΔMPC
B
Presynaptic fragments/NMJ
20
15
10
5
0
****
****
ns
C
Nerve terminals with NF varicosities (% total)
100
80
60
40
20
0
****
****
ns
D
AChR fragments/NMJ
10
8
6
4
2
0
****
****
ns
SMN2 1-copy Smn^WT
SMN2 2-copy Smn^ΔMPC
SMN2 1-copy Smn^ΔMPC

**Figure 3**

Morphological deterioration in NMJs of adult SMN2 1-copy $Smn^{\Delta MPC}$ mice. (**A**) Immunostaining of NMJs in TA muscle of SMN2 1-copy $Smn^{WT}$, SMN 2-copy, and SMN2 1-copy $Smn^{\Delta MPC}$ mice at P56 with anti-NF (Green), anti-synaptophysin (Blue), α-Btx staining AChR (Red). Scale bars, 20 μm. The confocal images of NMJs showed fragmentation and bouton-like NF varicosities (indicated by arrowheads) in the SMN2 1-copy $Smn^{\Delta MPC}$ mice. (**B-D**) The NMJs of the SMN2 1-copy mutant displayed fragmented presynapse (**B**), endplate (**D**), and NF varicosities (**C**) compared to SMN2 1-copy $Smn^{WT}$ and SMN2 2-copy $Smn^{\Delta MPC}$ mice (n = 3-5 mice in each genotype; Presynaptic fragments & AChR fragments: Brown–Forsythe and Welch ANOVA with Games-Howell's test; NF varicosities: 1-way ANOVA with Tukey's post hoc test). ns; not significantly different. ****$p < 0.0001$. All box-and-whisker plots show the median, interquartile range, minimum, and maximum. For the bar graph, error bars show s.e.m.

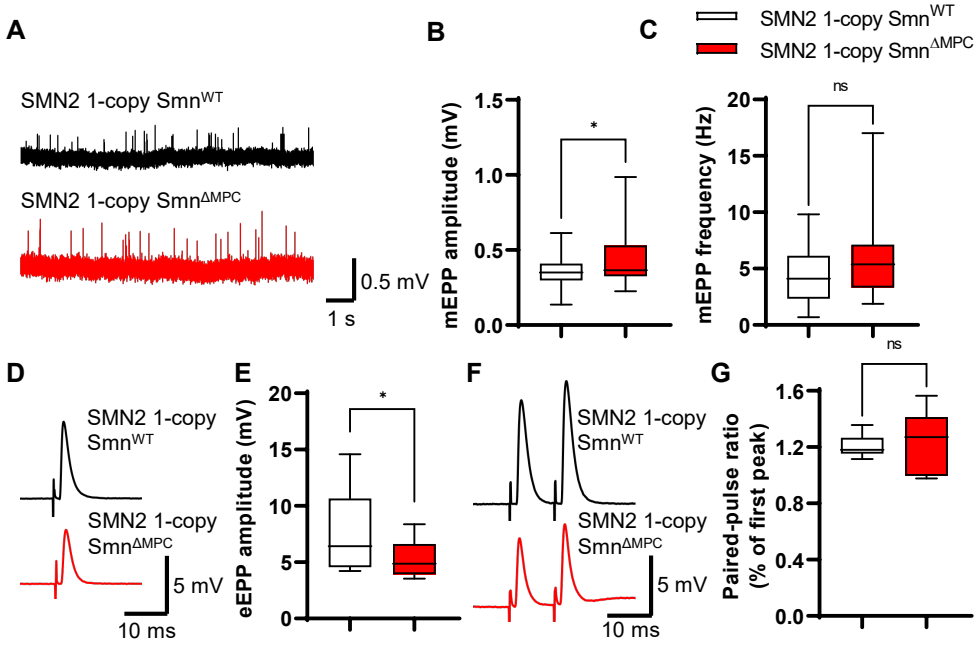
A
SMN2 1-copy Smn^WT
SMN2 1-copy Smn^ΔMPC
0.5 mV
1 s
B
mEPP amplitude (mV)
1.5
1.0
0.5
0.0
*
C
SMN2 1-copy Smn^WT
SMN2 1-copy Smn^ΔMPC
mEPP frequency (Hz)
20
15
10
5
0
ns
D
SMN2 1-copy Smn^WT
SMN2 1-copy Smn^ΔMPC
5 mV
10 ms
E
eEPP amplitude (mV)
20
15
10
5
0
*
F
SMN2 1-copy Smn^WT
SMN2 1-copy Smn^ΔMPC
5 mV
10 ms
G
Paired-pulse ratio (% of first peak)
1.6
1.2
0.8
0.4
0.0
ns

**Figure 4**

Reduced presynaptic neurotransmission ability in the NMJs of SMN2 1-copy $Smn^{\Delta MPC}$ mice. **(A)** Representative traces of mEPP from SMN2 1-copy $Smn^{\Delta WT}$ (top) and SMN2 1-copy $Smn^{\Delta MPC}$ (bottom) mice. **(B-C)** SMN2 1-copy mutant's NMJs showed an increase in mEPP amplitude and no differences in mEPP frequency (1-copy control, n = 25, 9 mice; 1-copy mutant, n = 21, 8 mice; Unpaired t-test with Welch's correction). **(D)** Representative traces of eEPP from SMN2 1-copy $Smn^{\Delta WT}$ (top) and SMN2 1-copy $Smn^{\Delta MPC}$ (bottom) mice. **(E)** The mutant's NMJs showed a stronger amplitude of eEPPs (1-copy control, n = 12, 4 mice; 1-copy mutant, n = 12, 3 mice; Unpaired t-test with Welch's correction). (**F**) Representative traces of paired-pulse response from SMN2 1-copy $Smn^{\Delta WT}$ (top) and SMN2 1-copy $Smn^{\Delta MPC}$ (bottom) mice. **(G)** Paired-pulse response was not different between SMN2 1-copy control and mutant NMJs, indicating a comparable neurotransmitter release probability (1-copy control, n = 8, 3 mice; 1-copy mutant, n = 6, 3 mice; Unpaired t-test with Welch's correction). The electrophysiological recording was performed in the EDL muscle at P56. ns; not significantly different. *$p < 0.05$. All box-and-whisker plots show the median, interquartile range, minimum, and maximum.

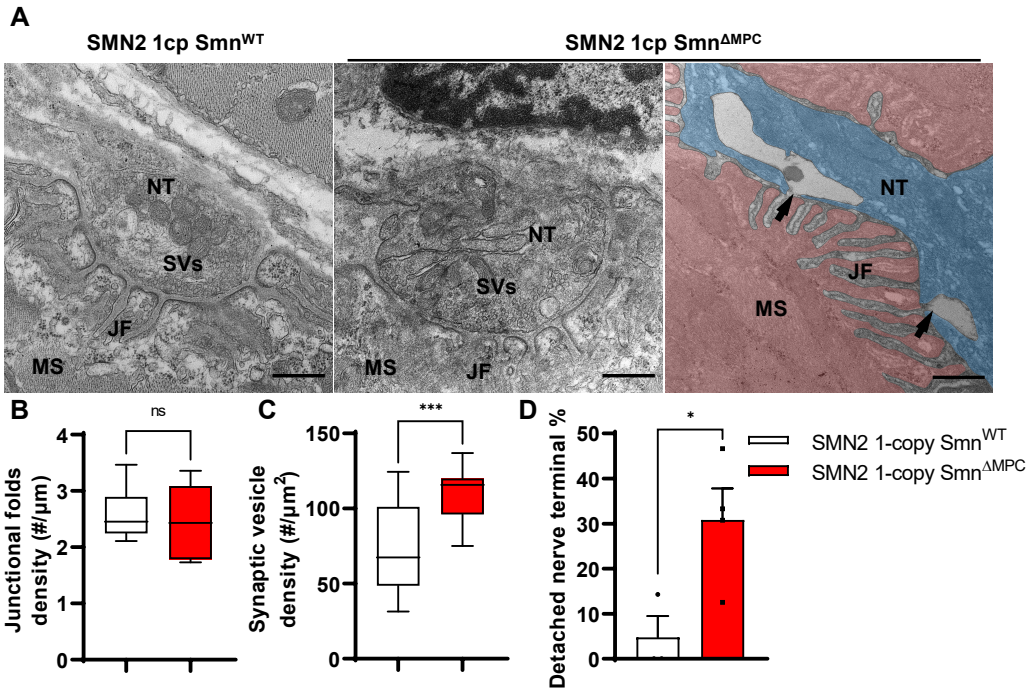
A
SMN2 1cp Smn^WT
SMN2 1cp Smn^ΔMPC
NT
SVs
JF
MS
NT
SVs
MS
JF
NT
JF
MS
B
ns
Junctional folds density (#/µm)
0
1
2
3
4
C
***
Synaptic vesicle density (#/µm²)
0
50
100
150
D
*
Detached nerve terminal %
0
10
20
30
40
50
SMN2 1-copy Smn^WT
SMN2 1-copy Smn^ΔMPC

**Figure 5**

Abnormal nerve terminal ultrastructure in SMN2 1-copy mutant. **(A)** Representative TEM images from NMJs of SMN2 1-copy $Smn^{\Delta WT}$ and SMN2 1-copy $Smn^{\Delta MPC}$ mice at P56. Scale bars, 500 nm. Nerve terminal (NT; indicated by the blue zone). Synaptic vesicles (SVs). Muscle fiber (MS; indicated by the red zone). Endplate junctional folds (JF). Nerve terminal detachment (indicated by arrow) was observed in SMN2 1-copy $Smn^{\Delta MPC}$ mice. **(B)** The density of junctional folds in the NMJ of SMN2 1-copy $Smn^{\Delta MPC}$ mice no significant change compared to the control, whereas (**C**) the density of synaptic vesicles was increased (n = 3-4 mice in each genotype; Unpaired t-test with Welch's correction). (**D**) The detachment of the nerve terminal occurs more frequently at the NMJ of mutants (n = 3-4 mice in each genotype; Unpaired t-test with Welch's correction). ns; not significantly different. $*p < 0.05$; $***p < 0.001$. All box-and-whisker plots show the median, interquartile range, minimum, and maximum. For the bar graph, error bars show s.e.m.

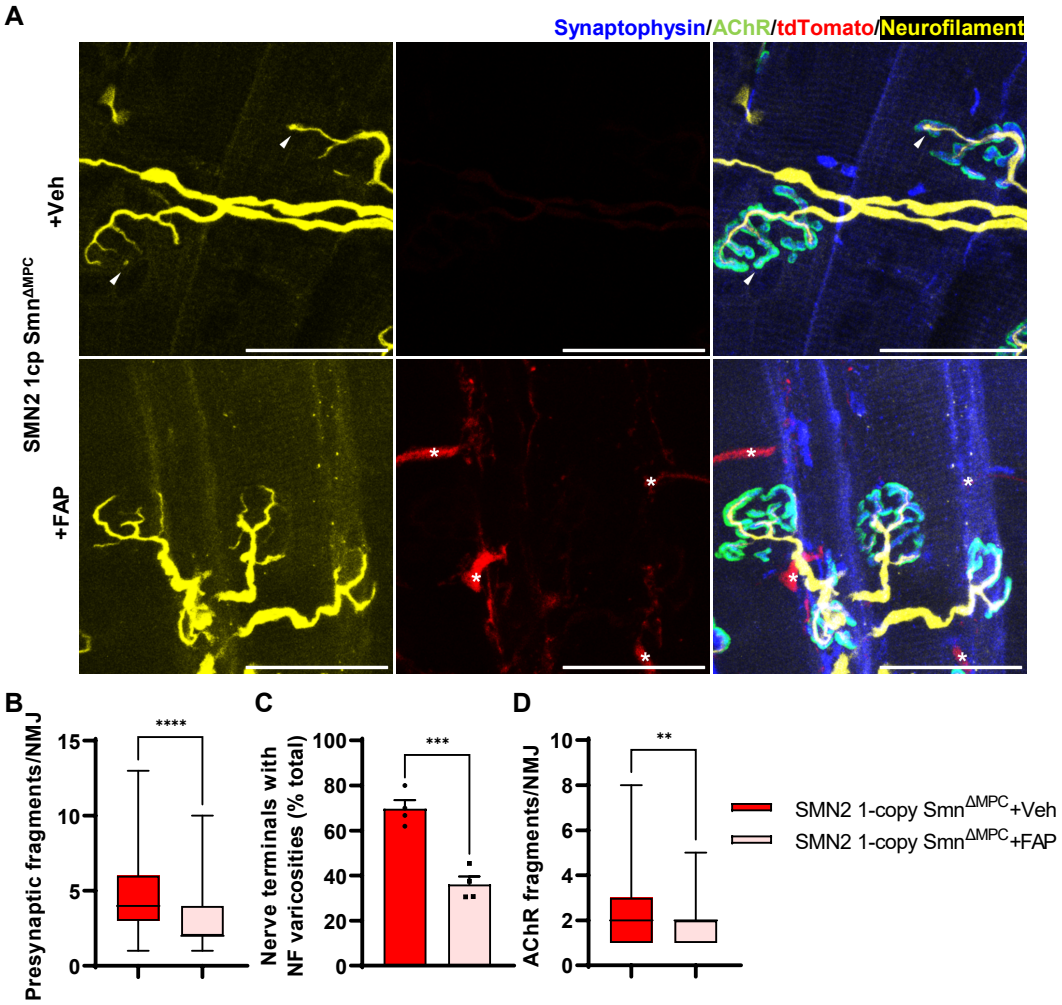
A
Synaptophysin/AChR/tdTomato/Neurofilament
SMN2 1cp SmnΔMPC
+Veh
+FAP
B
Presynaptic fragments/NMJ
****
C
Nerve terminals with NF varicosities (% total)
***
D
AChR fragments/NMJ
**
SMN2 1-copy SmnΔMPC+Veh
SMN2 1-copy SmnΔMPC+FAP

**Figure 6**

Improved postnatal NMJ development in the TA muscle of SMN2 1-copy $Smn^{\Delta MPC}$ mice following healthy FAPs transplantation. (**A**) Immunostaining of NMJs in $tdTomato^{+}$ FAPs-transplanted TA muscle (+FAP) and vehicle-treated contralateral muscle (+Veh) in SMN2 1-copy $Smn^{\Delta MPC}$ mice at P56 with anti-NF (Yellow), anti-synaptophysin (Blue), α-Btx staining AChR (Green), and tdTomato fluorescence (Red). Scale bars, 40 μm. The images revealed NF varicosities (indicated by arrowheads) in the +Veh NMJs. The tdTomato+ FAPs (marked by asterisks) were transplanted into +FAP NMJs, which exhibited (**B**) decreased presynaptic fragmentation, (**C**) NF varicosities, and (**D**) AChR fragmentation compared to +Veh NMJs. (n = 4 mice in each group; Unpaired t-test with Welch's correction). ns; not significantly different. $^{**}p < 0.01$, $^{***}p < 0.001$, $^{****}p < 0.0001$. All box-and-whisker plots show the median, interquartile range, minimum, and maximum. For the bar graph, error bars show s.e.m.